Title
Resonant soft X-ray techniques to resolve nanoscale magnetism

Author
Kortright, Jeffrey B.

Publication Date
2005

To be included as chapter in:
Modern techniques for characterizing magnetic materials
Kluwer Academic, Y. Zhu, Editor (9/20/04)

Resonant soft x-ray techniques to resolve nanoscale magnetism

Jeffrey B. Kortright
Materials Sciences Division
Lawrence Berkeley National Laboratory
Berkeley, California 94720 USA

1. Introduction

The soft x-ray spectral region contains important core levels of 3*d* transition and rare earth elements and so has emerged as a powerful spectral region in which to study magnetism in a variety of materials [1]. While some spectroscopic techniques are relatively mature in this spectral range, others are still under development. This chapter reviews a variety of evolving soft x-ray techniques as applied to the study of magnetism and magnetic materials. Emphasis is given to entirely photon based techniques that, compared to techniques detecting photoelectrons, can probe relatively deeply into samples and are compatible with strong and varying applied fields. Emphasis is also placed on techniques that can resolve magnetic structure either in depth or laterally in samples, rather than just providing spatially averaged properties.

The soft x-ray spectral range extends roughly from 100 eV to 2500 eV, and is often defined as that region where the path length of x-rays is insufficient to propagate in air at atmospheric pressure. This strong soft x-ray absorption has made this spectral range one of the last to be exploited to study magnetic materials, since specialized sources, optical elements, and instrumentation are necessary for such measurements [2]. Paradoxically perhaps, this strong absorption indicates large interaction cross-sections, especially at certain core levels, where magneto-optical effects can be larger than in any other spectral range. Synchrotron radiation sources generally provide the polarized soft x-rays needed for these studies, and are now common enough to provide reasonable access. Essentially all optical and scattering techniques common in the near-visible and x-ray spectral ranges have been extended into, or sometimes rediscovered in, the soft x-ray range. The coupling of these large, resonant magneto-optical effects with these various techniques is discussed here.

The following sections review fundamental characteristics of resonant magneto-optical spectra at x-ray core levels before introducing different approaches to apply these effects in different ways. Since modern magnetic materials are typically chemically and magnetically heterogeneous, often down to nanometer length scales, it is natural to categorize techniques by their ability to resolve such structure both in depth and laterally. For example, direct measurements of transmitted (forward scattered) beams average both laterally and in-depth throughout the illuminated area. Specular reflection techniques average over lateral structure, but can provide depth resolution in different ways. Diffuse scattering and diffraction, in transmission or reflection geometry, can resolve lateral structure and can also have variable depth sensitivity. Partially coherent scattering provides an ensemble average over structure, while coherent scattering retains details of local structural information. Finally, zone-plate microscopy provides direct images of local chemical and magnetic structure. Recent advances in each of these areas are discussed and compared below.

2. Core resonant magneto-optical properties

Optical and magneto-optical (MO) properties relevant to soft x-ray measurements are briefly reviewed here. First, geometrical conventions used in this chapter are defined in Figure 1 showing a generalized scattering event. Incoming and scattered wavevectors

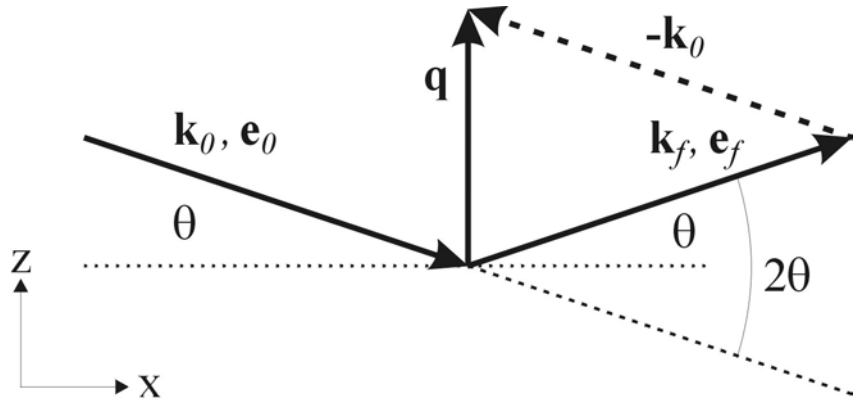

Figure 1. Vectors relevant to the scattering process. The sample can be of arbitrary form.

$\mathbf{k}_0$ and $\mathbf{k}_f$ define a scattering plane containing the scattering vector $\mathbf{q} \equiv \mathbf{k}_f - \mathbf{k}_0$. The magnitude $|\mathbf{q}| = (4\pi \sin\theta)/\lambda$, where 2θ is the total scattering angle and λ is the x-ray wavelength, is the spatial frequency probed in a scattering measurement. Structural information can be obtained only along $\mathbf{q}$ and is averaged perpendicular to $\mathbf{q}$. In the soft x-ray range $\lambda \approx 0.5 - 10\,nm$ and we can probe spatial frequencies corresponding to real-space distances as small as $\sim 2\pi / q = \lambda / 2$ or $\sim 0.2 - 2\,nm$. This ability to resolve nanometer-scale structure is one important feature of soft x-ray magneto-optical measurements. The wavevectors have associated polarization unit vectors $\mathbf{e}_0$ and $\mathbf{e}_f$ that are important in determining how charge and magnetic effects manifest in measurements. We define the Cartesian coordinate system with $\mathbf{z} \parallel \mathbf{q}$, so the $\mathbf{x} - \mathbf{z}$ plane defines the scattering plane in Figure 1.

The generalized scattering event in Figure 1 can be measured in transmission, specular reflection, or off-specular reflection geometry. The terms Faraday and Kerr are used here to designate transmission and reflection geometries, respectively, partly as a reminder of the distinct geometries used by these pioneers of MO effects. The sample magnetization **M**(x, y, z) is considered to potentially exhibit spatial variation in both direction and magnitude with position the sample. From MO effects in the near visible spectral range we adopt the terminology longitudinal, transverse, and polar to describe scattering measurements in which **M** is predominantly along **x**, **y** or **z**, respectively.

We can equally well describe the polarization ($\mathbf{e}_0$ and $\mathbf{e}_f$) of incident and scattered fields via orthogonal linear or circular components. Orthogonal linear components are referenced with respect to the scattering plane; $\mathbf{e}_\sigma$ has the electric field component always normal to the scattering plane ($\parallel \mathbf{y}$), while for $\mathbf{e}_\pi$ it is in the scattering plane ($\parallel \pm\sin\theta\ \mathbf{x} + \cos\theta\ \mathbf{z}$). Orthogonal circular components are referenced with respect to the directions $\mathbf{k}_0$ and $\mathbf{k}_f$. For right and left circular polarization $\mathbf{e}_0$ is given by $\mathbf{e}_+ = \dfrac{(\mathbf{e}_\sigma + i\mathbf{e}_\pi)}{\sqrt{2}}$ and $\mathbf{e}_- = \dfrac{(\mathbf{e}_\sigma - i\mathbf{e}_\pi)}{\sqrt{2}}$, respectively. Below we adopt linear or circular

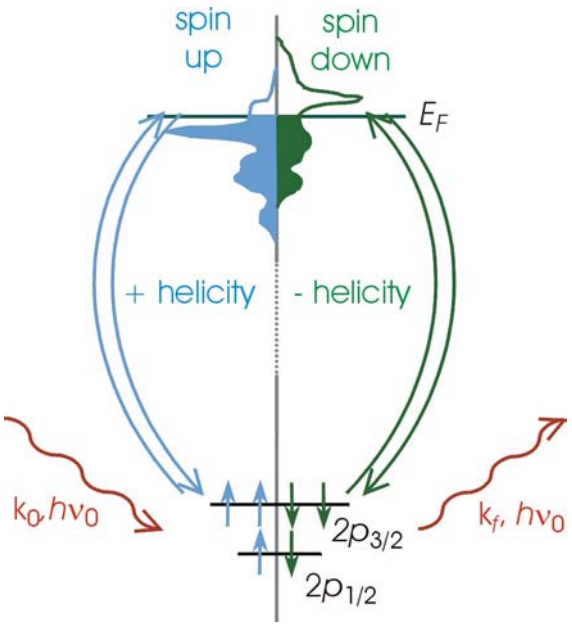

Figure 2. Quasi-elastic resonant scattering at with x-ray energies tuned to sharp, spin-orbit split core levels exhibit large magneto-optical effects through coupling to spin-polarized, empty intermediate states.

bases to describe $\mathbf{e}_0$ and $\mathbf{e}_f$ according to which provides the simplest description of the phenomena under consideration.

2.1. The resonant atomic scattering factors – theoretical description

The complex index of refraction $n(\lambda)$ and dielectric tensor $\boldsymbol{\varepsilon}(\lambda)$ are valid descriptions of optical and MO properties of matter in the x-ray spectral range. However, the atomic scattering factor $f(\lambda, q)$ provides a more fundamental, microscopic description, since it resolves the optical properties into the contributions of individual atoms and ions, and indeed their individual electronic states that constitute the sample. This elemental, electronic state specificity is another powerful aspect of core-resonant x-ray scattering measurements. Explicit polarization effects associated with distinct resonant charge and magnetic effects are simply expressed in $f(\lambda, q)$, as seen below.

The resonant scattering process at an atomic core level is schematically depicted in Figure 2. While resonant second-order matrix elements allow for many complex processes such as resonant inelastic scattering and fluorescence [3] we are concerned here with quasi-elastic scattering in which scattered and incident photons have the same energy. Detectors that operate in the soft x-ray range typically cannot discriminate between elastic and inelastic scattering, and grating spectrometers are needed to clearly resolve inelastic events. The varied scattering events discussed below are dominated by elastic scattering.

The atomic scattering factor is generally expressed as

$$f(\lambda,q) = f^0(q) + f'(\lambda,q) + if''(\lambda,q) \equiv f_1(\lambda,q) + if_2(\lambda,q)$$

containing a non-resonant term (f^0) and real and imaginary resonant terms (f' and f'') that are related through a Kramers-Kronig dispersion relation [4]. Refractive (real) terms are collected in f_1 and absorptive terms in f_2 [5]. $f(\lambda,q)$ is essentially the Fourier transform of the atomic electron density as sensed by radiation with wavelength λ. The *q* dependence results from the shape of the atomic electron density, although for the relatively large λ in the soft x-ray range the atoms scatter as points and this dependence is typically ignored. The resonant terms represent the sum of all allowed transitions within the scattering atom, which are spread throughout the spectrum for a given element, and vary systematically with atomic number [5]. Sensitivity to the electronic structure of, and immediately surrounding, the scattering atom results from the resonant absorption, and often yields valuable information about the distribution of electrons as well as their spin and orbital moments, as discussed below.

Quantum mechanical calculations identify many distinct resonant contributions to scattering at a given atomic core level [6], and the general expression for $f(\lambda,q)$ above effectively groups these together in f' and f''. We consider only electric dipole transitions, as higher order terms that may be significant in the hard x-ray spectral range are expected to be negligible in the soft x-ray range. Retaining only non-resonant pure charge and resonant charge and magnetic terms, all of which are much larger than non-resonant magnetic terms [6, 7] yields 3 leading resonant terms with distinct dependencies on $\mathbf{e}_0$ and $\mathbf{e}_f$. Together with the non-resonant charge term the scattering factor becomes

$$\begin{aligned} f(\lambda) = (\mathbf{e}_f^* \cdot \mathbf{e}_0)\left\{\frac{3}{8\pi}\lambda[F_{11} + F_{1-1}] - r_e Z\right\} \\ + \frac{3}{8\pi}\lambda\left\{i(\mathbf{e}_f^* \times \mathbf{e}_0)\cdot\mathbf{m}[F_{1-1} - F_{11}] + (\mathbf{e}_f^* \cdot \mathbf{m})(\mathbf{e}_0 \cdot \mathbf{m})[2F_{10} - F_{11} - F_{1-1}]\right\}. \end{aligned} \quad (1)$$

Here r_e is the electron radius, *Z* the atomic number, and **m** is a unit vector along the magnetization of the ion. The different F_{LM} terms are dipole matrix elements from initial to final states resolved into different spherical harmonics, and thus represent the spectral dependence of transitions between electronic states of specific symmetry, specific linear combinations of which are associated with distinct polarization dependencies. These polarization- and symmetry-specific contributions reveal how anisotropies in bonding as well as spin polarization can lead to anisotropic optical and magneto-optical properties. Indeed, in single crystals with reduced symmetry, measurements of the anisotropy of resonant scattering factors can provide information about the anisotropy in state-specific anti-bonding orbitals [7]. While the expression above was developed explicitly for localized atomic or ionic final states, these basic terms are also found in theoretical descriptions of atomic scattering factors in itinerant metallic systems described by band structure.

Most of the materials considered here are not single crystals, and we choose to simplify the scattering factor expression as

$$f(\lambda) = p_c(\mathbf{e}_0, \mathbf{e}_f) f_c(\lambda) + p_{m1}(\mathbf{e}_0, \mathbf{e}_f, \mathbf{m}) f_{m1}(\lambda) + p_{m2}(\mathbf{e}_0, \mathbf{e}_f, \mathbf{m}) f_{m2}(\lambda). \qquad (2)$$

Here f_c represents the resonant and non-resonant charge scattering, f_{m1} the resonant magnetic scattering 1st order in **m**, and f_{m2} the resonant magnetic scattering 2nd order in **m**. Corresponding polarization prefactors p_c, p_{m1} and p_{m2} contain the distinct polarization dependence of these terms resulting from the interaction of $\mathbf{e}_0$ with the vector spherical harmonics describing the transitions in (1). $p_c = \mathbf{e}_f^* \cdot \mathbf{e}_0$ is the well-known Thompson polarization dependence for a free electron. First order $p_{m1} = -i(\mathbf{e}_f^* \times \mathbf{e}_0) \cdot \mathbf{m}$ depends on 2θ, $\mathbf{e}_0$ and $\mathbf{e}_f$, and **m**, and is non-zero for circular polarization when $\mathbf{e}_0$ and $\mathbf{e}_f$ have the same helicity, or for linear polarization for $\sigma \rightarrow \pi$, $\pi \rightarrow \sigma$, or $\pi \rightarrow \pi$ scattering. Second order $p_{m2} = (\mathbf{e}_f^* \cdot \mathbf{m})(\mathbf{e}_0 \cdot \mathbf{m})$ depends on the projections of **m** with $\mathbf{e}_0$ and $\mathbf{e}_f$, and varies generally with orthogonal linear polarization. The terms optical, charge, and chemical scattering refer to f_c, while magneto-optical and magnetic scattering refer to f_{m1} and f_{m2}. However one must always consider how both charge and magnetic terms contribute to measured signals. First order MO effects include magnetic circular dichroism (MCD) and magnetic circular birefringence that yields rotation of linearly polarized light in the Faraday and Kerr geometries. These typically are the dominant MO effects in ferromagnetic (FM) materials, and are absent in compensated antiferromagnetic (AF) materials. Second order terms yield magnetic linear dichroism (MLD) that is present in compensated antiferromagnets and can be significant in ferrimagnets and high-anisotropy ferromagnets. Since f_{m2} is generally small compared to f_{m1} for metallic ferromagnets, it is common to ignore f_{m2}, as is done for the most part here.

The linear basis ($\mathbf{e}_\sigma, \mathbf{e}_\pi$) for $\mathbf{e}_0$ and $\mathbf{e}_f$ is a common choice in describing magnetic scattering [8, 7, 9]. However the circular basis ($\mathbf{e}_+, \mathbf{e}_-$) can bring added simplicity, since, according to (2) there is no polarization mixing in the scattering process, while there is mixing when using the linear basis. Adopting the circular basis and ignoring f_{m2}, the scattering factor simplifies to $f_\pm = p_c f_c \pm p_{m1} f_{m1}$, where $\pm$ refers to opposite helicity. For small 2θ and longitudinal **m**, we have $f_\pm \cong f_c \pm f_{m1}$. The asymmetry $f_+ - f_- \cong 2 f_{m1}$ gives just the first order magnetic part and the average $(f_+ + f_-)/2 = f_c$ gives just the charge part of the scattering factor [10]. While these simple expressions hold for these scattering *amplitudes*, we see below that the asymmetry and average of scattered *intensities* measured with opposite helicity are not so simply related to magnetism and charge because of interference of their amplitudes in the scattering process.

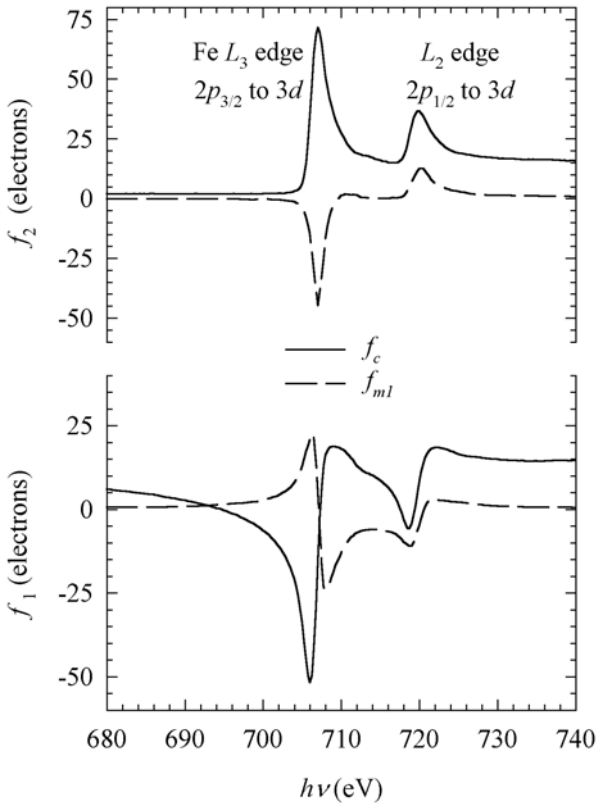

Figure 3. Measured charge (f_c) and first order magnetic (f_{m1}) scattering factors for Fe across its $L_{2,3}$ edges. The imaginary (f_2) and real (f_1) parts are related through Kramers-Kronig dispersion relations. (From Ref. 10.)

2.2. The Fe scattering factors across the $L_{2,3}$ edges

Particularly large resonant effects in f_c are expected to occur at absorption edges that couple sharp core levels to partially filled empty levels at and above the Fermi level via dipole-allowed transitions. When the core levels are spin-orbit split and the empty states are spin-polarized, large resonant magnetic effects in f_{m1} is expected. For the $3d$ transition elements, relevant L_2 and L_3 edges couple initial $2p_{1/2}$ and $2p_{3/2}$ levels to the spin-polarized $3d$ levels in the 500 – 1000 eV range. For rare-earth elements, relevant edges with strong resonances include M_4 and M_5 edges ($3d_{3/2}$, $3d_{5/2} \rightarrow 4f$) in the 850 – 1600 eV range, N_4 and N_5 edges ($4d_{3/2}$, $4d_{5/2} \rightarrow 4f$) in the 100 – 200 eV range. Weaker rare-earth resonances occur at the N_2 and N_3 edges ($4p_{1/2}$, $4p_{3/2} \rightarrow 5d$) in the 200 – 400 eV range, and M_2 and M_3 edges ($3p_{1/2}$, $3p_{3/2} \rightarrow 5d$) in the 1200 – 2200 eV range. All of these edges fall in the soft x-ray spectral range, making it especially attractive for resonant magnetic studies. Also interesting are the rare earth L_2 and L_3 edges in the 5,700 – 10,300 eV hard x-ray spectral range (see Chapter 5).

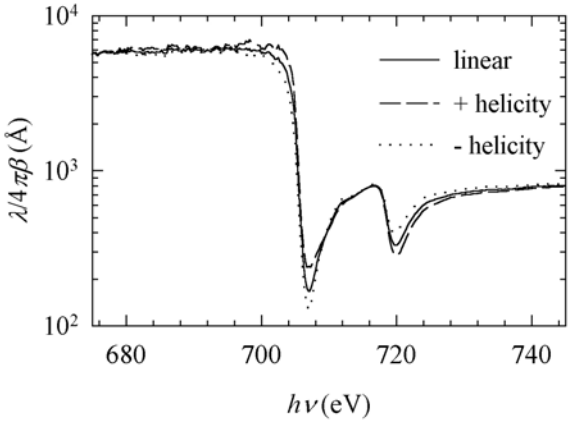

Figure 4. The 1/*e* penetration depth at normal incidence for Fe across its $L_{2,3}$ edges shows strong helicity dependence. Magnetization is assumed to be normal to the surface. (From Ref. 10.)

Experimentally determined values of f_c and f_{m1} for elemental Fe across its $L_{2,3}$ edges [10] in Figure 3 are dominated by strong white line absorption at the sharp core levels, and corresponding strong resonances in the refractive contributions. The results for Fe are representative of the other 3*d* transition metals (Cr – Ni) of interest in magnetic materials, whose white line strengths decrease as the 3*d* states fill with increasing *Z*. Similar results for selected rare earth elements are available in the literature [11]. As will be seen, it is these large resonant changes in both f_c and f_{m1} that enable many new measurements in this spectral range. For elemental Fe, f_{m2} shows very weak resonant enhancement compared to f_{m1} [10].

The resonant spectral behavior of f_c and f_{m1} can be important for many reasons, ranging from experiment planning to interpretation of various scattering results including absolute determination of spin and orbital moments via sum rules. Because their resonant values can depend strongly on local chemical environment and hence can vary significantly with sample, their careful determination for specific samples studied can be important. Here we use these values for Fe to draw some general conclusions for soft x-ray studies of magnetic materials by considering the behavior of the skin depth and critical angle for total external reflection vs. energy near the 2*p* core levels.

The relation between the complex index of refraction *n* and the atomic scattering factors is useful in some of these considerations. For a homogeneous, multicomponent phase the index is given by $1 - n(\lambda) = \sum_i N_i r_e \lambda^2 f_i(\lambda,0)/2\pi$, where different species *i* have different $f_i(\lambda,0)$ and number density N_i, and r_e is the electron radius. For elemental Fe, considering only the first order magnetic term leads to three limiting cases for *n* [10]. Zero f_{m1} contribution (only charge scattering) yields n_0 and corresponds to propagation normal to **M**. Maximum f_{m1} contribution of opposite sign yields n_+ and

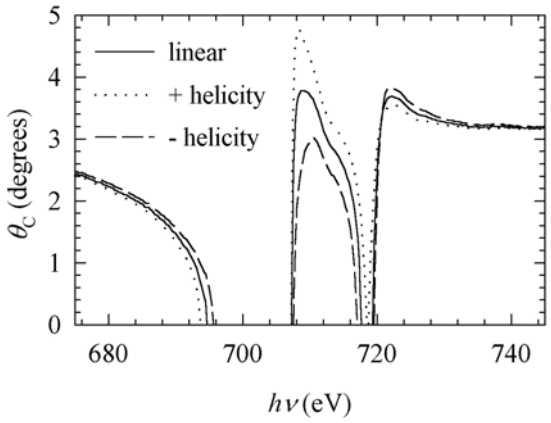

Figure 5. The critical angle for total external reflection evaluated for different polarizations assuming magnetization is saturated in the longitudinal direction in the surface plane. (From Ref. 10.)

$n_{\_}$, corresponding to circular polarization propagating parallel and antiparallel to saturated **M**. Each can be written $n = 1 - \delta - i\beta$ where β is the absorption index and δ the refractive contribution. The penetration depth for the electric field intensity at normal incidence, $\lambda / 4\pi\beta$, is strongly dependent on $h\nu$ and polarization across the 2*p* spectrum, as seen in Figure 4. Below the L_3 edge radiation penetrates hundreds of *nm* into an Fe sample, independent of polarization. Strong L_3 absorption significantly reduces penetration in a polarization dependent way to 13 and 24 *nm* for the opposite helicity circular components. Away from normal incidence, skin depth scales as $\sin\theta$ until near the critical angle for total reflection where refractive effects come into play. Thus at θ = 15°, commonly used to study samples with in-plane **M**, the penetration depth is only 3 and 6 *nm* for the circular components. Below it is seen that this energy dependent penetration depth can be used to obtain depth-resolved information.

Large optical and MO effects occur near the critical angle for total external reflection, $\theta_C = \sqrt{2\delta}$, that is plotted for +/- helicity (charge plus/minus magnetic) and linear (charge only) scattering in Figure 5. The dispersive resonances associated with the L_3 and L_2 lines are strong enough that θ_C vanishes when $f' < -Z$ electrons and $\mathrm{Re}[n] > 1$, in which case incident wave fields refract *into* the sample rather than toward the sample surface. In the transition from total external to total internal reflection, the optical properties pass through the zero refraction condition when δ passes through 0. Not only are the resonant charge refractive effects quite large, but the magnetic counterparts are likewise large, as seen by the distinct differences in θ_C for the different polarizations. Both the reflected intensity and the phase change on reflection (which varies by π from $\theta = 0$ to $\theta = \theta_C$) are strong functions of polarization (or **M** direction), and so can produce striking MO effects in experiments operating near this angular range.

Especially when working in reflection geometry, changes in θ, $h\nu$, $\mathbf{e}_0$, and $\mathbf{M}$ can have a striking influence on the shape of *q*-resolved scattered signals because of changes in the effective sample volume resulting from these changes in penetration depth and θ_C, and from changes in magnetic scattering amplitudes. These optical and magneto-optical effects can overshadow effects due, for example, to spatial structure variation of interest in a specific measurement [10]. Thus it is important to utilize realistic resonant scattering factors in modeling experimental results, so that these effects can be clearly distinguished from possible structural signals of interest.

3. XMCD and related spectroscopies

In this section spectroscopy is narrowly defined to represent the energy dependence of either the imaginary (f_2) or the real (f_1) part of f_c, f_{m1}, and f_{m2}. Specifically, we limit consideration first to measurements of $f_{2,c}$ and $f_{2,m1}$, and $f_{1,m1}$. Here we are primarily concerned with measuring the spatially averaged values, rather than their possible variation with position. In subsequent sections we consider spectroscopic aspects of techniques to explicitly resolve the spatial variation of magnetic structure. In the case of scattering techniques, measured energy spectra generally depend on both the real and imaginary parts of the scattering factors, often in complex ways.

Near edge x-ray absorption fine structure (NEXAFS) or x-ray absorption (XAS) spectra ($f_{2,c}$) are of interest because they provide a direct measure of the density of unoccupied states that can be used to study systematic changes in materials and can be compared with theoretical calculations of electronic structure [12]. For example, the strength of the Fe L_3 and L_2 white lines in Figure 3 is a measure of the unoccupied 3*d* and 3*s* states accessible from the 2*p* level via dipole selection rules. The high symmetry of Fe atoms in the bulk bcc structure yields relatively featureless L_3 and L_2 lines, although reduced crystal field symmetry generally introduces multiplet splitting in the 3*d* states that can show up as pronounced, characteristic NEXAFS features [13]. NEXAFS spectra thus provide a useful experimental indicator of general trends in local atomic or ionic configurations. Theoretical interpretation of such spectra must proceed with care, as the absorption process itself complicates the measurement of ground state (unexcited) electronic structure, since this structure relaxes to screen the core hole produced in the absorption event, and scattering effects of the outgoing photoelectrons can influence spectral shapes [12, 7].

3.1. XMCD sum rules and applications

Magnetic dichroism spectra are measured in accordance with the polarization dependence of p_{m1} and p_{m2}. While x-ray MLD (XMLD) [14] was observed before x-ray MCD (XMCD) [15] in the x-ray spectral region, XMCD is sensitive to ferromagnetic moments and thus is more generally utilized than XMLD. Using circular polarization with reversed helicity or magnetization, XMCD is defined as $\mathrm{Im}[f_+ - f_-] = 2p_{m1}f_{2,m1}$,

where p_{m1} emphasizes that measurements sense the projection of **m** on $\mathbf{k}_0$. The XMCD spectrum ($f_{2,m1}$) for Fe is in the upper panel of Figure 3.

Beyond element-specific detection of ferromagnetic moments and their qualitative variation among samples, sum rules can yield quantitative measures of elemental spin [16] and orbital moments [17]. The sum rules use the areas under the L_3 and L_2 XMCD peaks, A_3 and A_2, respectively, to determine the effective spin moment $m_{spin}^{eff} \propto A_3 + A_2$ and the orbital moment $m_{orb} \propto A_3 - 2A_2$ [18]. Determination of the absolute value of these elemental moments requires a value for the number of holes in the 3*d* shell n_{3d}^h that is generally not known. Experimentally n_{3d}^h is proportional to the sum of the areas of the L_3 and L_2 white lines in f_c. The ratio m_{orb} / m_{spin}^{eff} is independent of n_{3d}^h. m_{spin}^{eff} is an effective spin moment because, according to the sum rules, the spectra leave unresolved a contribution from the magnetic dipole moment. The sum rules have been used to obtain values for spin and orbital moments consistent with those expected for Fe, Co, and Ni [18, 19].

The ability to measure m_{orb} is a powerful aspect of XMCD spectroscopy, especially since orbital moments are sensitively related to magnetocrystalline anisotropy in the bulk and at interfaces in thin films. This sensitivity has advanced our understanding of the reorientation transition from in-plane to perpendicular magneto-crystalline anisotropy (PMA) in ultra thin films by revealing enhanced orbital moments associated with interfaces [20, 21], as predicted originally by Néel [22]. This reorientation transition is generally thought to occur as the interfacial contribution to the total anisotropy, generally favoring perpendicular anisotropy, overcomes the bulk contribution favoring in-plane anisotropy, with decreasing film thickness. XMCD studies applying the sum rules have observed large enhancements in orbital moments in ultrathin ferromagnetic films grown on or sandwiched between normal metals [23, 24, 25, 26, 27]. Several studies suggest that this enhanced interfacial m_{orb} has a distinct perpendicular anisotropy [20, 21] in films thin enough to exhibit PMA, while another points out the difficulty of resolving anisotropy of orbital from spin moments because of spin-obit coupling [28]. One study observed an enhanced interfacial m_{orb} with in-plane orientation in a thicker film with overall in-plane anisotropy [27].

In addition to the enhanced interfacial orbital moments, XMCD has revealed other important phenomena relating to magnetism in ultrathin films and at buried interfaces. One example is induced moments in nominally non-magnetic, ultrathin spacer layers such as Pt, Pd, and Cu when layered with ferromagnetic layers such as Co [29, 24, 30]. Another example is a significant increase (or change, more generally) in the size of the L_3 and L_2 white lines of 3*d* ferromagnetic layers at interfaces with non-metals [27, 27], indicating an increase in n_{3d}^h consistent with charge transfer out of the 3*d* states. Yet another example is the observation of magnetic dead layers at interfaces. While interfacial Co in Co/Pt multilayers shows enhanced orbital and spin moments, Ni interfaces with Pt show regions of reduced or no magnetism [31, 32].

All of these examples point to the conclusion that significant hybridization generally occurs at buried interfaces, with resulting redistribution of electrons in ways that radically alter electronic and magnetic properties potentially on both sides of the

interface. It is also clear that XMCD and NEXAFS provide valuable capabilities to resolve these and other changes in electronic structure at buried interfaces. Of course, bulk properties of thin films are also studied beneficially with these spectroscopies. Magnetic semiconductors are one such class of materials, where induced moments of Ga and As host species are observed in $(Ga_{1-x}Mn_x)As$ [33], and Co moments are observed in dilute Co anatase $(Ti_{1-x}Co_x)O_2$ films [34].

3.2. Sensitivity of different absorption techniques

The above examples raise questions regarding the depth-sensitivity of soft x-ray XAS and XMCD measurements. How, for example, can sensitivity to buried interfaces be obtained? For the most part, these studies have determined that specific properties are intrinsic to interfaces by studying ultrathin films as their thickness decreases; interfacial effects are reasonably inferred to dominate in the thin limit. But the measured signals have only finite sensing depths, and, since subtle changes in spectral shapes and intensities are sometimes used to draw conclusions, it is important to consider the systematics of depth sensitivity. Three different modes are commonly used to measure XAS and XMCD in the soft x-ray range; total electron yield, fluorescence, and transmission.

By far the most common means to measure absorption in the soft x-ray range is by total electron yield, which is dominated by low energy secondary electron emission from the sample. In practice it is often easier to measure not the emitted electrons directly, but their complement given by the sample drain current flowing into the sample. Low energy secondary electrons have short escape depths $l_e \cong 2-4\ nm$ that limit the available information depth. The x-ray penetration length $l_x = \frac{4\pi\beta}{\lambda}\sin\theta$ for grazing incidence angle θ is generally large compared to l_e, but can be comparable to or less than l_e at the strong white lines in absorption spectra (above). Thus, even though l_e is small and essentially constant with λ, the strong energy dependence of $l_x(\lambda)$ imparts an energy dependence on the excitation rate of secondary electrons with depth than can significantly influence intensity of absorption features. Correction factors for these well-known saturation artifacts must be applied to obtain realistic values for spin and orbital moments from sum rules [19]. This in turn requires knowledge of $l_x(\lambda)$, as well as its polarization dependence. Electron yield detection can be compatible with varying applied magnetic fields, provided care is taken to ensure that all emitted electrons contribute to the signal.

Even though its cross-section is weak in the soft x-ray region, fluorescence detection mode is also used to obtain NEXAFS and XMCD spectra, and is clearly compatible with strong and varying applied fields. The fluorescence signal escape depth l_f is much greater than l_e, although similar considerations and corrections for the interplay between l_f and $l_x(\lambda)$ are applicable. A more fundamental concern is whether the *L* fluorescence signal is a true measure of the overall absorption, since the fluorescence cross-section is not necessarily equal for different multiplets [35, 36]. A practical concern relates to the very low cross-section (< 1 %) for fluorescence in general

in the soft x-ray range [37], that does not preclude the possibility that resonant elastically scattered photons may be detected along with fluorescence. While careful detector positioning based on p_c can minimize elastic charge scattering, p_{m1} shows that this is not effective for resonant magnetic scattering. Thus a grating spectrometer is the best means to ensure that only fluorescence photons are detected.

Standard transmission absorption measurements are possible provided samples can be synthesized with appropriate thickness [10]. Silicon nitride membranes provide semi-transparent substrates on which thin films can be deposited, and freestanding films can also be used. Fortuitously, the optimal thickness for transmission measurements (one or two absorption lengths) is in the thickness range of many magnetic thin film systems of current fundamental and technological interest. As in other spectral regions, saturation artifacts in transmission absorption measurements become important especially at strong absorption lines when samples are too thick [10]. Transmission measurements sense the entire sample thickness, and are compatible with applied fields.

3.3. Polarizing optical elements

Complete characterization of x-ray MO effects, just as in the near-visible spectral range, requires the ability to measure not just the intensity but also the phase (or polarization) of incident or scattered beams. At a minimum, rotating linear polarizers are needed to measure a beam's degree of linear polarization (P_L). Ideally quarter wave retarders would also be available to distinguish possible unpolarized (P_U) from circularly polarized radiation and thereby unambiguously determine the degree of circular polarization (P_C). In practice, synchrotron radiation is inherently polarized so that $P_U = 0$, and P_C can be determined from $P_L^2 + P_C^2 = 1$.

Optics for the measurement and manipulation of polarization in the soft x-ray range are typically based on the polarization dependence of charge scattering [38]. According to p_c, the Brewster angle (minimum in reflectivity for $\mathbf{e}_0 = \mathbf{e}_\pi$) in the x-ray range is $\theta_B \cong 45^\circ$ where. Across the 100 – 2000 eV range the extinction ratio, or the reflectivity ratio of σ to π polarization, at θ_B is high (10^2 – 10^7), providing good polarization rejection for a linear polarizer. Reflectivity for the σ component is generally quite low (10^{-2} – 10^{-7}) for highly polished, semi-infinite mirrors, and to boost efficiency multilayer structures are used to create an interference peak at θ_B. In the 100 – 2000 *eV* range the period of such multilayers decreases from 8.8 *nm* to only 0.44 *nm*. Multilayer linear polarizers with periods down to ~ 0.6 nm have been fabricated and tested [39]. In the 500 – 1000 *eV* range including the *L* edges of the 3*d* transition metals, these polarizers typically have σ component reflectivity ~ 10^{-2} – 10^{-3} at the interference peak that is of order 1° (or $\Delta\lambda / \lambda \approx 0.01$) wide. To increase the polarizer bandwidth, translation along a period gradient [40], and operation at a range of angles near θ_B [41, 42] are used. Figure 6 shows a schematic of a tunable linear polarizer based on graded multilayer reflectors [46]. The multilayer film is deposited on the reflecting surface with its period gradient normal to the scattering plane. Translating the multilayer along its gradient then tunes its interference peak at θ_B to occur at the desired x-ray energy. Alternatively, one can operate at fixed multilayer period or incidence angle and correct

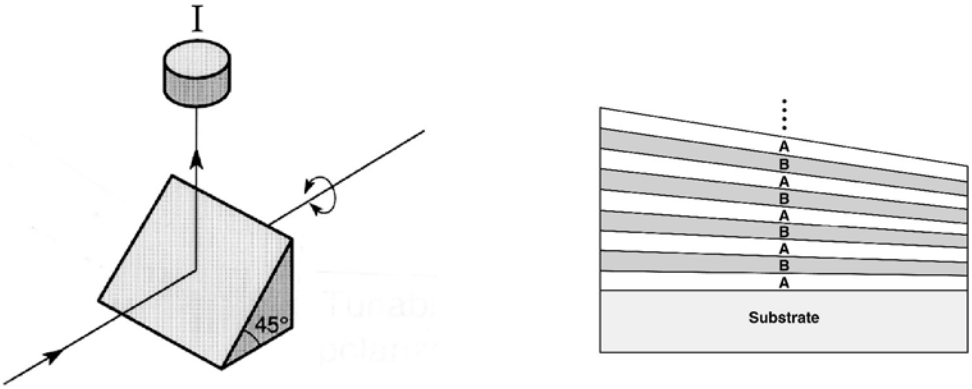

Figure 6. A Brewster angle polarizer in the soft x-ray ranges operates by reflection through 90° into an intensity detector (left). The entire assembly rotates around the incident beam. Efficiency is improved by operating at the interference maximum of a multilayer interference film. A lateral gradient in multilayer period (right) allows the interference peak to be tuned in energy by translating the gradient normal to the scattering plane. (From Refs. 46, 40.)

any energy dependent measurements for the reflectivity spectrum of the multilayer. Such linear polarizers are used both to measure the polarization of $\mathbf{e}_0$ and to monitor polarization changes in $\mathbf{e}_f$ resulting from magneto-optical effects.

Phase retarding optics, such as quarter wave plates, can also be made for use in the soft x-ray range. One approach uses multilayer interference structures either in transmission or reflection, operating near the interference peak where optical standing waves yield different phase changes on scattering for σ and π components [43, 44]. Resonant MO effects themselves have also been used to create elliptically polarizing filters, whose utility is limited to very near the resonant core levels [45].

3.4. X-ray Faraday effect measurements

Transmission (Faraday) measurements of rotation of linearly polarized incident radiation provide a direct measure of magnetic circular birefringence, the refractive counterpart of MCD. Multilayer polarizers must be used to measure this rotation directly, and can also measure any ellipticity induced on transmission through the sample [46, 10]. Faraday rotation spectra yield $f_{1,m1}$ directly, and $f_{2,m1}$ indirectly via the dispersion relation. While transmission measurements of XMCD can yield erroneous results especially for thick samples due to the presence of higher harmonics in the beam, multilayer polarizers suppress unwanted radiation outside of their narrow bandpass. The Faraday rotation signal can be large several eV below the L_3 edge, where absorption is minimum. These factors enable Faraday rotation spectra to sense element specific magnetization behavior in thicker samples than might be possible using the direct absorption channel.

Because the sample volume is well defined in Faraday rotation measurements, the magnetic rotary power or specific rotation (Verdet constant) thus measured can be

compared across spectral ranges for a given material. Specific rotation measured at the L_3 white line in Fe is up to 6 x 10^5 *deg/mm* [47, 10]. This is more than an order of magnitude larger than observed for Fe in any other spectral region, and attests to the value of x-ray MO studies using sharp core resonances.

3.5. Theoretical spectral calculations

Theoretical calculations of XMCD and Faraday effect signals have been made by different groups, and generally show good qualitative agreement with experimental measurements. Theories generally calculate the spin-polarized density of states using either an atomic or band formalism. Absorption spectra are obtained by summing transitions allowed by dipole selection rules ($\Delta l = \pm 1$ and $\Delta j = 0, \pm 1$ for l, j quantum numbers) weighted by the projected density of empty states and by the square of the radial matrix elements.

Enhanced (and suppressed) interfacial moments at interfaces have been observed in calculations [24, 48]. Effects of induced moments at nominally non-magnetic sites due to magnetic neighbors have been calculated [49], as have field-induced magneto-optical effects in paramagnetic solids [50]. The importance of spin polarization and spin splitting in 2*p* core states has been established through comparisons of measurements with theory [51, 52]. XAS and XMCD spectra of Fe_3O_4 and related structures have been calculated and found to be in good agreement with experimental measurements [53].

4. X-ray magneto-optical Kerr effect (XMOKE) – specular reflection

The magneto-optical Kerr effect (MOKE) refers to specular reflection geometry. Lateral structure within the illuminated area is averaged in measurements of the specular beam. Core resonant x-ray MOKE (XMOKE) adds elemental specificity, shorter wavelengths for *q*-resolved studies of in-depth interference effects, and tunable penetration depth. These features imply that XMOKE effects should be better suited to study depth-variations in magnetic behavior in layered thin film systems than their near-visible MOKE counterparts. The term XMOKE is utilized here to refer to all resonant magnetic effects measured in the specularly reflected beam, acknowledging that many researchers have used different terminology.

4.1. Theoretical considerations

All theoretical considerations made for MOKE measurements in the near visible spectral range [54, 55], such as intensity and phase effects in different settings (longitudinal, transverse, polar) generally extend into the x-ray range. Thus it is straightforward to extend formalisms for near-visible MOKE into the x-ray range, requiring only that optical and MO properties embodied by f_c, f_{m1}, and f_{m2} be properly translated into refractive indices and dielectric tensor elements used in these formalisms [10]. Again we limit consideration to f_c and f_{m1} contributions to these MO effects.

To describe XMOKE effects it is important to adopt formalisms that explicitly allow for depth variations in chemical and magnetic structure, *i.e.*, for layered structures

[56, 57]. In these descriptions, matrices are formulated to describe the complex amplitudes of reflected and transmitted fields at each interface, as well as matrices describing how complex field amplitudes change on propagation through each layer. Suitable matrix manipulation thus allows the evaluation of various MOKE effects for arbitrary $\mathbf{k}_0, \mathbf{e}_0$.

Such MOKE formalisms typically utilize the linear basis ($\mathbf{e}_\sigma$, $\mathbf{e}_\pi$), and yield a matrix $\begin{pmatrix} r_{\sigma\sigma} & r_{\sigma\pi} \\ r_{\pi\sigma} & r_{\pi\pi} \end{pmatrix}$ describing the reflectance properties of the sample and containing the magnetic properties of the model structure. Operating on $\mathbf{e}_0$ then yields the amplitude of the reflected field. With $\mathbf{e}_0 = \mathbf{e}_\sigma$, *e.g.*, the scattered field is given by $\begin{pmatrix} r_{\sigma\sigma} & r_{\sigma\pi} \\ r_{\pi\sigma} & r_{\pi\pi} \end{pmatrix}\begin{pmatrix} 1 \\ 0 \end{pmatrix} = \begin{pmatrix} r_{\sigma\sigma} \\ r_{\pi\sigma} \end{pmatrix}$, where $r_{\sigma\sigma}$ gives the non-rotated (charge) amplitude and $r_{\pi\sigma}$ the rotated (magnetic) amplitude. The reflected Kerr intensity is $r_{\sigma\sigma}^2 + r_{\pi\sigma}^2$ and the polarization of the reflected field is described by $r_{\pi\sigma} / r_{\sigma\sigma} = \phi_\sigma' + i\phi_\sigma''$ where ϕ_σ' is the Kerr rotation and ϕ_σ'' the induced ellipticity of the linearly polarized incident beam.

Arbitrarily complex layered systems of magnetic and non-magnetic materials can be treated with such recursive formalisms by defining a sufficient number of layers to account, for example, for depth varying magnetic properties across a single FM layer. Parameters of such models can be varied to fit measured data to provide direct insight into depth resolved behavior. Accurate values of resonant f_c and f_{m1} are essential in this modeling process, as deduced magnetic structures are meaningful only in reference to their assumed or measured values.

4.2. Exchange-spring heterostructures

Early studies of XMOKE effects include demonstrations of the various expected polarization and intensity effects [58, 59, 60, 61, 62, 63, 64, 11, 65, 66]. Because of the added complexity of measuring polarization dependent effects, such as Kerr rotation and ellipticity, many early studies consider only intensity effects. These studies emphasize the large size of the Kerr effects across relevant core levels, and have primarily been concerned with first order MO effects, although second order effects have also been observed in reflection geometry [67]. The rapid variation of these large MO effects with λ and θ can be at first puzzling, or useful when understood in the context of model calculations using realistic values for resonant optical properties.

Here we review early studies of exchange-spring heterostructures that provide new information about their depth-resolved magnetic properties. Figure 7 illustrates a magnetic bi-layer system in which a high anisotropy (hard) FM layer is exchange-coupled to a lower anisotropy (soft) FM layer. These systems are the basis of some of today's magnetic storage devices [68], and are of interest as model systems to study FM-FM exchange coupling and thereby composite magnets with potentially larger stored energy than single-phase magnets [69, 70]. The illustration shows the expected response to a small reverse *H*; initially the top of soft layer reverses while the bottom is pinned by

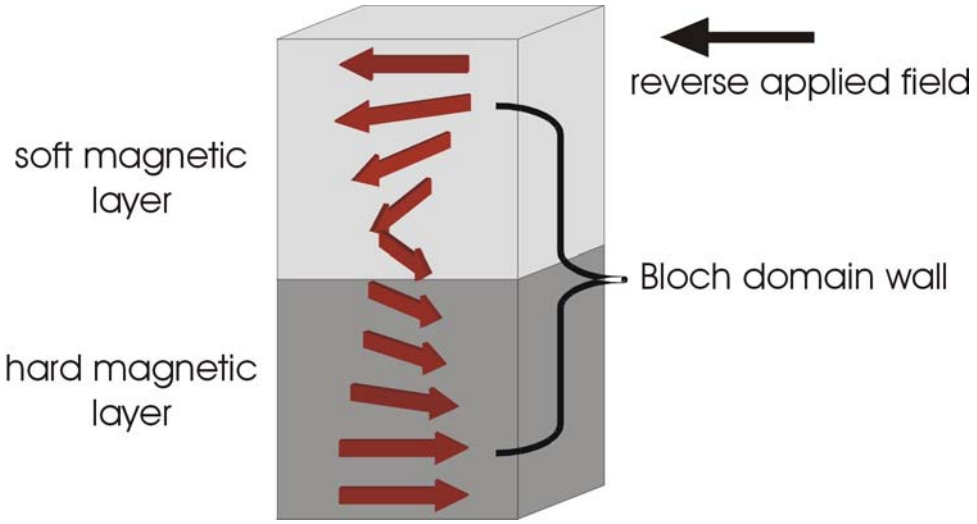

Figure 7. Exchange-spring heterostructures formed by exchange-coupled low (soft) and high (hard) anisotropy ferromagnetic films have useful and interesting properties. In a reverse applied field the soft layer switches more easily than the hard layer.

exchange coupling to the hard layer, producing a magnetization spiral (or Bloch domain wall) in depth in the film. At small H this partial switching is completely reversible (no hysteresis), hence the term exchange-spring. As H increases, eventually the hard layer switches completely. Theoretical models and macroscopic magnetization measurements observe a two-step reversal in such films [71], with low H_{rev} corresponding to the reversible initial switching of the soft layer, and with high H_{irr} corresponding to the switching of the hard layer. H_{irr} is reduced from the coercivity of an isolated hard layer, since the interfacial exchange softens the hard layer just as it hardens the soft layer.

While these general trends were clear prior to XMOKE studies, the details of how depth-dependent reversal proceeds was impossible to verify using techniques sensitive only to macroscopic behavior. Various aspects of resonant soft x-ray techniques make them useful in elucidating depth-dependent reversal in the different layers of such exchange-coupled systems.

Several measurements have focused on exchange-spring systems of general structure MgO(110)/buffer(t_A *nm*)/Sm-Co(t_B *nm*)/Fe(t_C *nm*)/cap(t_D *nm*), where the buffer and cap layers are either Cr or Fe and Cr or Ag, respectively, and thickness t_A, t_B, t_C, and t_D differ slightly [61 ,72]. The quasi-epitaxial nature of these samples yields an in-plane, uniaxial anisotropy. XMOKE measurements were made along the easy axis in longitudinal geometry (Figure 8) at small θ near both the Fe and Co $L_{2,3}$ resonances to probe the soft and hard layer **M** structure through minor and major hysteresis loops, always starting from saturation. Measured quantities include the Kerr intensity following reflection from sample as well as the raw Kerr rotation signal following reflection from a tunable linear polarizer.

The soft Fe layer is probed by tuning near the Fe $L_{2,3}$ resonances. Figure 9 shows XMOKE hysteresis loops from a sample with a 5 *nm* Cr cap layer and a 20 *nm* Fe layer

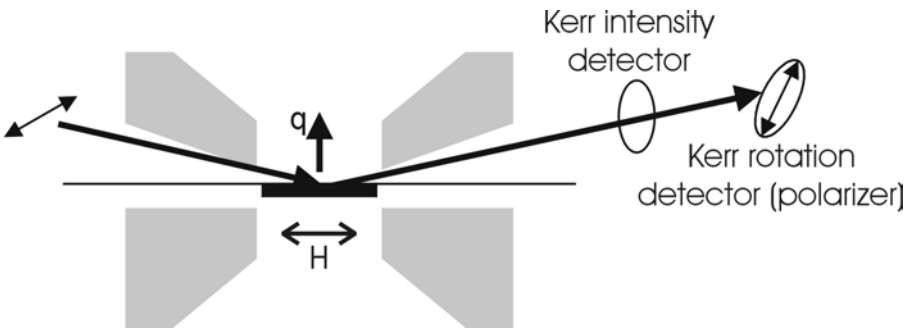

Figure 8. Experimental geometry for longitudinal XMOKE. The Kerr intensity is measured together with the Kerr rotation. If the intensity varies on magnetization reversal, the Kerr rotation signal must be normalized by this variation to obtain the true Kerr rotation.

measured at $\theta = 3.6^{\circ}$ with energy tuned 2.3 *eV* below the peak in the L_3 absorption line, where penetration depths are relatively large [61]. Data collected using both linear and near-circular polarizations ($P_C = 0.9$) were used.

We consider first the XMOKE results obtained with $\mathbf{e}_0 = \mathbf{e}_\sigma$ in the left panels of Figure 9. The raw Kerr rotation loop (top panel), measured with polarizer's scattering plane at 45° with respected to sample's scattering plane about $\mathbf{k}_f$, shows a large intensity variation and asymmetric shape that, interpreted in isolation, could lead to mistaken conclusions. This is because the Kerr intensity signal (middle panel), measured before the polarizer, itself shows large changes through the loop. The Kerr intensity loop is symmetric with respect to **M**(**H**) reversal, showing a sharp jump at low *H*, followed by gradual changes and another jump at high *H*. These features are clearly associated with the onset of reversal by the top of the Fe layer at H_{rev}, a laterally coherent twist structure at intermediate *H*, and the high field switching of the hard layer at H_{irr}. The raw Kerr rotation signal, normalized by the Kerr intensity signal and converted to Kerr rotation angle, is in the bottom panel. This normalized Kerr rotation is now symmetric in *H*, and like the Kerr intensity shows the onset of soft-layer reversal, the evolution of the twist structure, and the switching of the hard layer with increasing *H*. The size of the Kerr angle is much larger than that typically observed in near-visible spectral regions.

The observation of a Kerr intensity signal is significant for different reasons. It is well known that transverse MOKE effects yield intensity changes for $\mathbf{e}_0 = \mathbf{e}_\pi$ polarization with changes in net transverse moment. While the measurement had $\mathbf{e}_0 = \mathbf{e}_\sigma$, strong Kerr rotation yields an induced π component as radiation penetrates into the sample that in turn yields the observed Kerr intensity signal. The net transverse moment yielding the Kerr intensity signal implies a largely coherent magnetization spiral of specific chirality, consistent with the quasi-epitaxial nature of the Sm-Co/Fe system. Similar XMOKE studies of polycrystalline FePt/NiFe exchange-spring couples do not observe a Kerr intensity signal under similar conditions, meaning that incoherent spin spirals equally populate both chiralities during reversal [73]. Thus, buy measuring both Kerr intensity

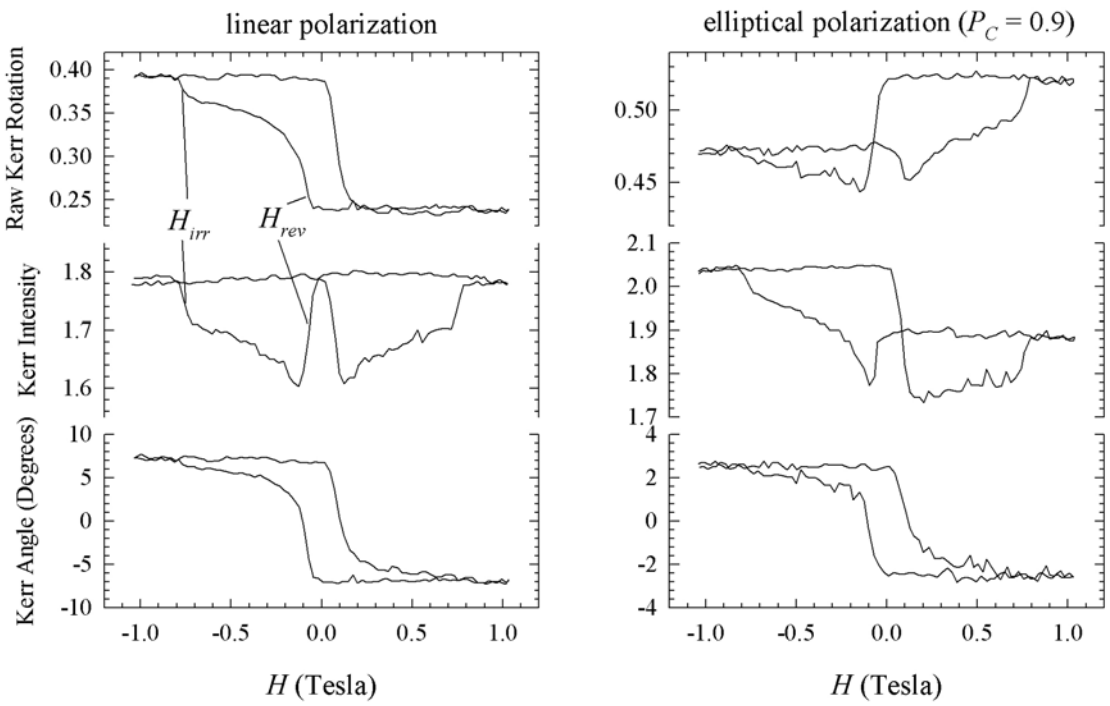

Figure 9. XMOKE data showing reversal of the soft Fe layer in a Sm-Co/Fe exchange-spring sample obtained by tuning near the Fe L_3 edge. Data at left are obtained with linear ($\mathbf{e}_\sigma$) incident polarization and at right with near circular polarization. Two-stage reversal of Fe is evident. (From Ref. 61.)

and Kerr rotation, we learn simultaneously about longitudinal and net transverse magnetization behavior.

It is instructive to compare the shapes of XMOKE signals measured using linear incident polarization with those measured using near-circular polarization. The right-hand panels in Figure 9 show the same signals as at left measured under the same conditions ($h\nu, \theta$), except using elliptical (P_C = 0.9) polarization. The Kerr intensity loop is now asymmetric in H, as expected since circular polarization has different reflectivity for oppositely oriented longitudinal M because the charge-magnetic interference term (below) is odd in M. The raw Kerr rotation loop is asymmetric in a different way than the Kerr intensity, but the normalized Kerr angle is again symmetric with an identical shape as that measured using $\mathbf{e}_0 = \mathbf{e}_\sigma$, although with reduced magnitude. The observation of any Kerr rotation might at first be surprising for nearly pure circular incident polarization. However, again the magnetization itself induces an increase in P_L as radiation propagates in the sample.

The sensitivity to longitudinal and net transverse **M** is clearly different for linear and circular polarization. The higher apparent symmetry of loops measured using linear polarization results because it is equivalent to a superposition of + and – helicity circular components. This allows for easier qualitative interpretation of linear polarization loops in terms of longitudinal and transverse M changes, provided that a polarizer is available to measure Kerr rotation.

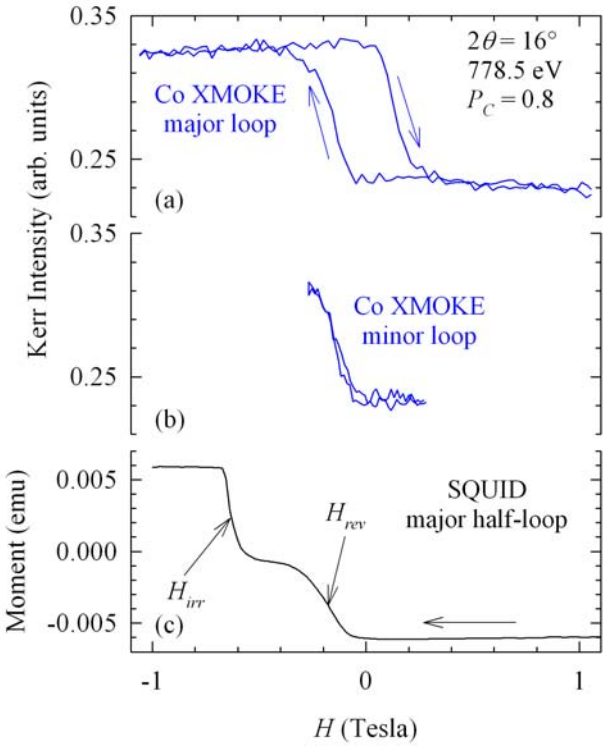

Figure 10. XMOKE loops (a & b) showing the reversal in a buried Sm-Co layer in a Sm-Co/Fe exchange-spring couple obtained with near circular polarization at the Co L_3 line. The SQUID major half-loop (c) shows the macroscopic reversal of the same sample. All loops start at positive saturation. (From Ref. 72.)

These qualitative interpretations of the behavior of longitudinal and net transverse moments associated with the spiral structure within the Fe layer can be more quantitatively established by modeling. By describing the spiral in the Fe layer using multiple thinner layers, the recursive XMOKE formalism above reproduces the shapes of the Kerr rotation and intensity loops [61]. Such modeling easily rules out the (unlikely) possibility that the spiral is pinned at the top, rather than the bottom surface of the soft layer, thereby providing depth resolution throughout the 20 nm Fe layer through measurements made at a *single*, low θ and fixed $h\nu$. This relatively good penetration results because $h\nu$ is tuned just below the L_3 line, where absorption is minimized and $\mathrm{Re}[n] > 1$ so that radiation refracts into the Fe layer rather than toward it's surface. Tuning to the peak of the Fe L_3 line maximizes absorption and changes the refractive conditions to substantially reduce penetration into the Fe layer. Loops measured under these conditions can be sensitive to just the upper region of the soft Fe layer, showing only the low H reversal as the spiral is formed, with no signal resulting from the pinned region near the interface [61].

Direct sensitivity to the buried hard layer can also be obtained by tuning to the Co $L_{2,3}$ edges to monitor the Co reversal in the Sm-Co layer. This is done for a sample having structure MgO(110)/Fe(20 *nm*)/Sm-Co(80 *nm*)/Fe(20 *nm*)/Ag(20 *nm*), operating at $\theta = 8.0^\circ$, $P_C = 0.8$, and with $h\nu$ tuned to the peak of the L_3 line where Co MCD is

largest [72]. Figure 10 shows a major and minor Kerr intensity loop together with half of a major loop measured with a SQUID magnetometer from the same sample. The Co XMOKE loops are interesting for two reasons. First, these loops show a large, *reversible* Co signal at H_{rev} when the reversible spiral is formed in the soft Fe layer. Second, the major loop shows no signal at $H_{irr} \sim 0.6$ Tesla when the hard layer switches irreversibly. This later observation is understood to result from the limited (~ 2 *nm*) penetration in the thick Sm-Co layer with $h\nu$ tuned to the Co L_3 peak. Together the two XMOKE loops imply that the reversible twist structure penetrates significantly into the hard layer as soon as it is formed in the soft layer, as was also observed for another exchange-spring system [73]. Such information is not readily available from standard magnetometry.

4.3. Opportunities

The above examples obtain depth-resolved information either from modeling the shape of hysteresis loops at fixed θ , from element-specificity, and from varying the skin depth by tuning $h\nu$ near a sharp resonance. Other approaches to gain depth resolution are available. One is to grow a compatible chemical marker layer at different depths within a magnetic multilayer, and tune $h\nu$ to the core level of the marker layer [73]. Another is to measure systematic XMOKE effects vs. q and fit these variations with realistic models of magnetic variations in depth [61, 65]. The resonant enhancements in chemical and charge scattering generally tend to enhance interference effects in layered films, enabling these q-resolved signals to be fit with relatively simple models involving magnetic variations with depth. An extreme example of this approach is to generate optical standing waves in a multilayer structure and tune the position of the standing waves to resolve magnetic structure within a fraction of the standing wave period [27, 74].

XMOKE techniques are generally applicable to any layered system. Further systematic studies of exchange-coupled FM-FM systems can be expected. These techniques can sense uncompensated AF moments in exchange bias systems [75], and provide depth dependent reversal information in such systems, as shown by several early studies. Induced magnetism across non-magnetic interfaces, interface-induced changes in magnetic layers, and other proximity effects are examples of problems that will be beneficially studied with XMOKE in future studies.

5. Diffuse scattering and diffraction

While XMOKE provides depth resolution through different approaches, it averages over lateral structure (both chemical and magnetic) that is common in real systems. Topological interface roughness, grain boundaries, chemical segregation, and magnetic domains are distinct forms of heterogeneity, all of which give rise to scattering away from the specular beam in reflection geometry and away from the forward scattered beam in transmission geometry. The q resolved scattered intensity directly probes the spatial frequency spectrum of an ensemble of heterogeneities present in the sample. With q_{max} the highest spatial frequency measured, spatial resolution is given by $2\pi / q_{\max}$, or $\lambda / 2$ at backscattering. Tuning to core resonances dramatically enhances both chemical

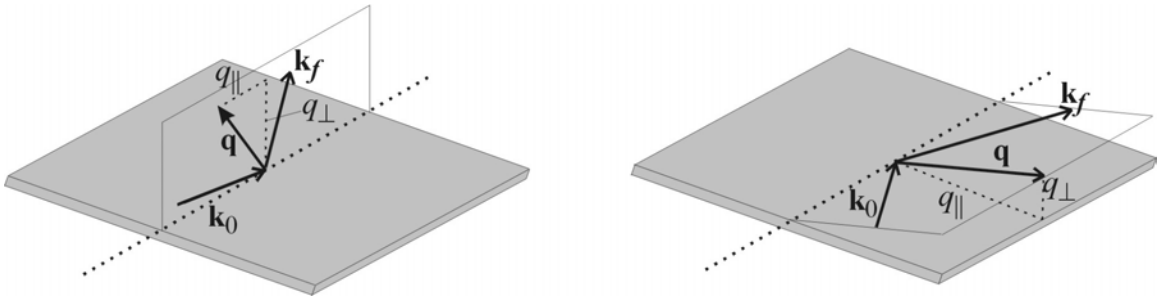

Figure 11. Reflection geometries of diffuse scattering utilize the in-plane component of the scattering vector to couple to lateral heterogeneity. At left the scattering plane (outlined) is normal to the surface, while at right it is strongly inclined toward the surface.

and magnetic contributions to scattered intensities, allowing the distinction of charge and magnetic structural that often co-exist without perfect correlation in real systems.

The first soft x-ray magnetic diffuse scattering studies used the off-specular reflection geometry to investigate magnetic and chemical surface roughness [76, 77]. In specular reflection geometry, **q** is strictly perpendicular ($q_\perp$) to the surface, and off-specular geometries yield an in-plane **q** component ($q_{\|}$) that can be varied to study in-plane heterogeneity. For a fixed scattering angle 2θ or total **q**, the partition of **q** into $q_\perp$ and $q_{\|}$ depends on how the scattering plane is oriented with respect to the sample surface; two limiting cases are shown in Figure 11. With the scattering plane normal to the surface it is difficult to get to large $q_{\|}$ values for small 2θ, while with the scattering plane at a small angle from the surface **q** is predominantly along $q_{\|}$. For a given sample the two geometries have different sensitivity to magnetic structure through their different $\mathbf{e}_0$ and $\mathbf{e}_f$. If measuring diffuse scattering using an apertured detector, scans of detector or sample angles trace out an intensity trajectory through reciprocal space. Alternatively a CCD detector can be positioned in the scattered beam as in Figure 12 to measure a range of $q_{\|}$ and $q_\perp$ for a given incident beam.

Such studies generally have used circular polarization with $\mathbf{e}_0 = \mathbf{e}_{+/-}$ in conjunction with reversed **M** to measure intensities I_+ and I_-, where + and – refer either to reversed helicity for fixed **H**, or *vise versa*. Both of these quantities typically decrease monotonically with $q_{\|}$. The difference $I_+ - I_-$ was interpreted initially as giving the magnetic intensity, and $(I_+ + I_-)/2$ as the charge (or chemical) scattering. Variations of the difference and average with $q_{\|}$ were then interpreted to represent the power spectra of magnetic and charge roughness. These initial studies found that $I_+ - I_-$ falls more quickly with $q_{\|}$ than does $(I_+ + I_-)/2$, and concluded that magnetic roughness has longer in-plane correlation lengths than chemical roughness. Studies have since pointed out that $I_+ - I_-$ actually corresponds to the charge-magnetic interference term [78]. In these measurements, $q_\perp$ can vary along with $q_{\|}$. Such variations in $q_\perp$ introduce

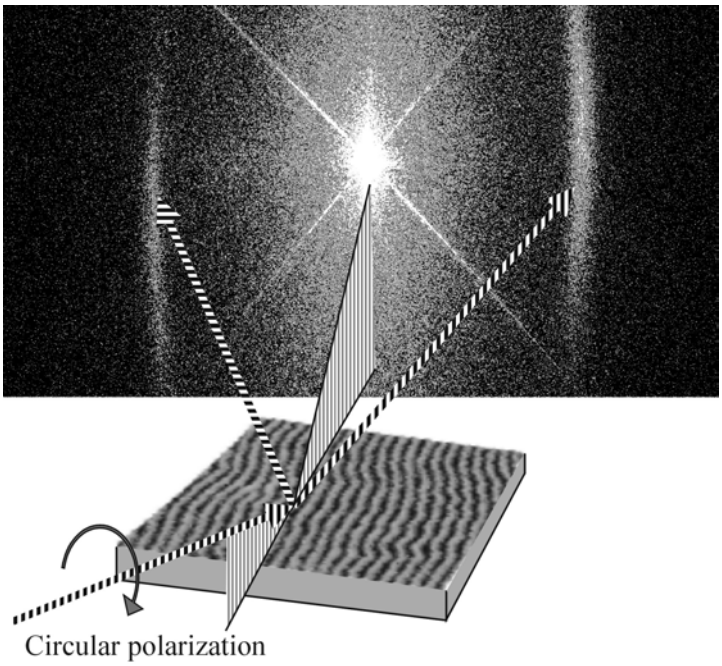

Figure 12. A CCD detector positioned in the specularly reflected beam can measure diffuse scattering with a range of $q_{\parallel}$ and $q_{\perp}$ corresponding to a range of scattering planes. The sample consists of oriented magnetic stripe domains. Positive and negative diffraction orders from the domains are on either side of the bright specular beam on the CCD detector. From Ref. 9 (used with permission).

variations in the specular reflectivity that modulates the scattered intensity from heterogeneities either at or below the surface [79, 10]. These variations can be particularly strong as $q_{\perp}$ approaches zero and eitherθ_i or θ_o approach θ_C. Since θ_C and penetration depths vary significantly with helicity and **M** (Figures 4 & 5), these optical and MO effects strongly influence the variation of $I_+ - I_-$ vs. $q_{\parallel}$. Thus care should be taken in interpreting its shape relative to that of $I_+ + I_-$.

5.1. Theoretical considerations

Questions such as these concerning the relative charge and magnetic contributions to scattered intensities $I(\mathbf{q},\lambda)$ can be analyzed with relatively simple formalisms based on the scattering factor (2). While f_{m2} scattering has been observed from antiferromagnets [80], $f_{m1} >> f_{m2}$ for ferromagnets and we limit consideration here to scattering from f_c and f_{m1} whose spatial variations generally differ. Here we adopt the circular basis and again use $f_{\pm} = p_c f_c \pm p_{m1} f_{m1}$.

A sample's scattering amplitude is generally written for opposite helicity circular polarization as $a_{\pm} = \sum_i f_{i\pm} \exp[i\mathbf{q}\cdot\mathbf{r}_i]$, where the sum is over all atoms in the sample volume that may or may not be magnetic. For simplicity consider that all atoms are

magnetic and of the same species. The intensity scattered in the Born approximation is then given by

$$I_{\pm}(q) = \sum_i \sum_j f_{i\pm}^* f_{j\pm} \exp[i\mathbf{q}\cdot\mathbf{r}_{ij}] = f_c^2 s_{c-c} + f_m^2 s_{m-m} \pm 2(f_{2c}f_{1m} - f_{1c}f_{2m})s_{c-m} \quad , \quad (3)$$

where partial structure factors $s_{c-c}(\mathbf{q})$, $s_{m-m}(\mathbf{q})$, and $s_{c-m}(\mathbf{q})$ describe the spatial distribution of charge-charge, magnetic-magnetic, and charge-magnetic correlations, respectively. Even for multi-component, mixed magnetic-nonmagnetic samples, the intensity can be grouped according to terms having p_c^2, $p_c p_{m1}$, and p_{m1}^2 polarization dependence, so the same 3 partial structure factors can be identified, although their weighting factors may be different. Thus there are always intensity contributions representing charge-charge, magnetic-magnetic, and charge-magnetic correlations. The orientations of the atomic moments $\mathbf{m}_i$ determine the strength of the magnetic contribution through p_{m1}. Since s_{c-m} and s_{m-m} are odd and even in helicity, respectively, it follows that $I_+ - I_- = 4(f_{2c}f_{1m} - f_{1c}f_{2m})s_{c-m}$ contains only the cross-term, as noted in Ref. 78. It also follows that $(I_+ + I_-)/2 = f_c^2 s_{c-c} + f_m^2 s_{m-m}$ contains the pure charge and pure magnetic contributions to the intensity [81]. Furthermore, if linear incident polarization were used, its scattered intensity $I_{lin} \equiv (I_+ + I_-)/2$ [81, 88].

These expressions reveal the importance of distinguishing between the charge-magnetic and the pure magnetic intensity contributions, both of which are magnetic in origin but behave very differently as applied fields change the magnetization distribution. At resonance, $|f_c|$ is generally greater than $|f_{m1}|$. Thus, if measuring scattering using circular polarization, one can expect large changes in intensity with **M(H)** reversal resulting from the $p_c p_{m1}$ term implicit in s_{c-m} since p_{m1} is odd in M. If linear polarization is used, much smaller changes in intensity are expected from the p_{m1}^2 term in s_{m-m}, and these changes are expected to be symmetric in **M(H)**. These features imply that the *q* dependence of the asymmetry $I_+ - I_-$ can provide information about magnetic structure, but in a form that is strongly field-modulated through cross-correlation with chemical structure information. Furthermore, I_{lin} vs. *q* provides information about pure magnetic structure, but only in the presence of a background of pure charge scattering. Thus, the difference in intensities $I_{lin} \equiv (I_+ + I_-)/2$ obtained at two different fields isolates changes in pure magnetic scattering, independent of any charge scattering whatsoever [81].

5.2. Perpendicular stripe domains in thin films

Magnetic domains and chemical grains, often present in thin films and bulk magnetic materials, are distinctly different forms of heterogeneity from magnetic and chemical topological surface roughness investigated in the earliest soft x-ray resonant magnetic scattering studies mentioned above. Such heterogeneities, in the form of up and down stripe domains in films with perpendicular anisotropy, illustrated in Figure 13, form an important class of samples in which resonant magnetic scattering has been extensively

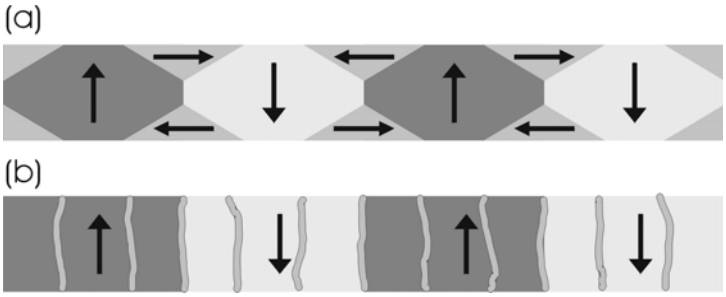

Figure 13. Schematic cross sections of magnetic stripe domains in thin films having perpendicular magnetic anisotropy, with arrows and shading indicating local magnetization directions. Relatively weak perpendicular anisotropy leads to surface closure domains as in (a). Possible chemical heterogeneity in the form of columnar grain boundaries or chemical segregation are indicated by irregular vertical lines in (b).

studied [82, 83, 84, 85, 86, 87, 88, 89]. Film systems with relatively weak perpendicular anisotropy tend to form surface closure domains, as in Figure 13a, that become difficult to study as the stripe domain widths decrease.

Off-specular reflection geometry studies of magnetic domains in FePt films with weak perpendicular anisotropy using detection geometries in Figure 11 (right) and Figure 12 reveal that the periodic domain structure forms a magnetic grating that scatters into a series of diffraction orders extending to + and – in $q_{\parallel}$ at fixed $q_{\perp}$ [82, 88]. Using circular polarization, the +/- asymmetry of these magnetic diffraction peaks is observed to switch with helicity reversal [83], indicating that in-plane **M** components are located at the perpendicular grain boundaries as in Figure 13a. The sum and difference of these magnetic intensities obtained with opposite helicity are observed to be quadric and linear in M [9], consistent with the simple model developed above. The incidence angle dependence of the asymmetry provides a measure of the depth of the surface closure domains and experimentally verifies the chiral nature of closure and stripe domains as in Figure 13a. These studies demonstrate how resonant magnetic scattering can resolve details of 3 dimensional magnetization structures in samples that are sufficiently ordered.

Co/Pt multilayer films have stronger perpendicular anisotropy (less pronounced surface closure domains), and provide a model system both to further test fundamental predictions of the simple scattering theory developed above and to study a wide range of magnetic phenomena that can be designed into these synthetic materials. Considering p_{m1} reveals that transmission geometry scattering measurements with **q** in the film plane, as in Figure 14, maximizes magnetic relative to charge scattering for studies of the spatial characteristics of magnetic domains in these systems. Such measurements are analogous to traditional small-angle x-ray scattering (SAS), but with added magnetic sensitivity.

Transmission SAS studies of Co/Pt multilayers reveal distinct magnetic and charge peaks resulting from magnetic domain and polycrystalline chemical grain structure, respectively [84]. Figure 15 shows $I_{lin}(q)$ measured with incident linear polarization tuned to the Co L_3 peak to yield resonant enhancements in both f_c and f_{m1}. At saturating field a peak at $q \cong 0.3\ nm^{-1}$ is observed. Near remanence a second peak

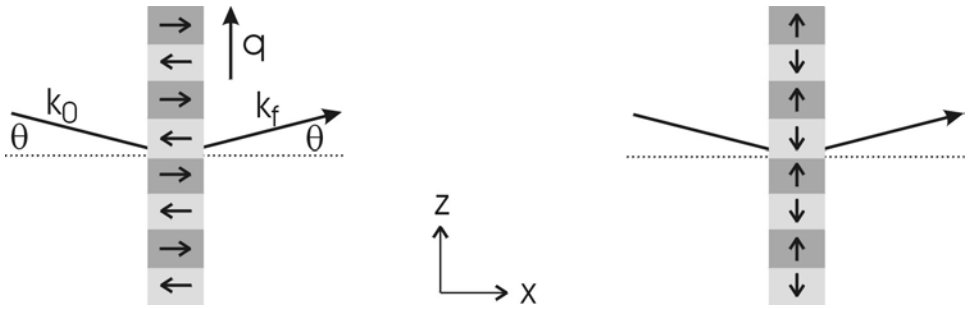

Figure 14. Transmission geometry to measure scattering from magnetic domains in thin films positions q in the film plane. Arrows indicate local magnetization directions. For small θ magnetic sensitivity is optimized for perpendicular magnetization as in (a). Reduced, but nonzero, sensitivity exists to in-plane magnetization structure as in (b).

appears at lower $q \cong 0.042\ nm^{-1}$. Disordered stripe domains are known to proliferate in the reversal of such films from magnetic force microscopy (MFM) and x-ray microscopy (XRM) images. Figure 16 shows an XRM image of domains in a similar film measured using an imaging zone-plate microscope (below) at the Co L_3 edge. In addition to the scattered intensity vs. q, Figure 15 shows the scaled power spectral density (PSD) functions obtained from the Fourier transform of the XRM domain image and from an atomic force microscope (AFM) surface height distribution. Both the field dependence of low-q peak in I_{lin} and its coincidence in position with the domain PSD indicate that it originates from the magnetic domains. The spatial wavelength $2\pi / q_{peak} = 150\ nm$ corresponds to the average up-down domain pair length scale. The AFM image shows height variations characteristic of polycrystalline grains, and the high-q scattering peak results from interference of scattering from adjacent polycrystalline grains.

A hysteresis loop of the diffuse scattering at the low-q peak is shown together with a visible MOKE hysteresis loop for this sample in Figure 17. The scattering is at a very small background level when the sample is saturated, rises abruptly at the nucleation of reverse domains, peaks near the coercive field, and falls to the background level at saturation. This comparison shows clearly that magnetic scattering is sensitive to a very different part of the hysteresis process than the MOKE loop, or any other hysteresis loop measuring nominally the *average* magnetization of the sample. Specifically, magnetic scattering measures *deviations from the average* magnetization with great sensitivity both to the field and spatial frequency dependence of these deviations. Scattering is thus an excellent tool to study magnetization structure present during complex reversal processes.

While the predominant magnetic and charge origin of the low- and high-q peaks, respectively, are without doubt, it is instructive to compare the energy dependence of the scattering at each peak with theoretical predictions (above) and measured values of f_c and f_{m1}. This is done in Figure 18, where the top and middle panels show energy scans (symbols) at the magnetic and charge peaks, respectively, collected both at saturation and at 0.1 Tesla where the magnetic domain scattering is most intense. The bottom panel

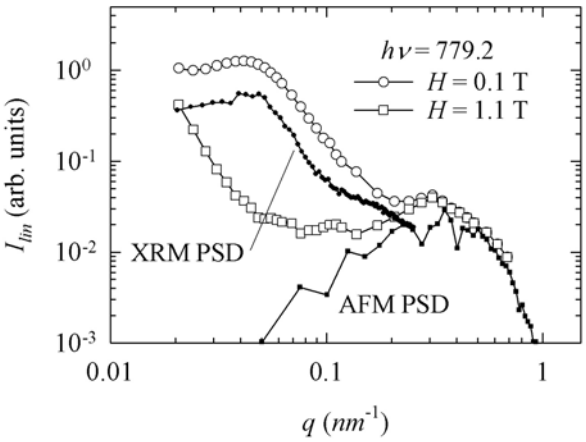

Figure 15. Scattered intensity from a Co/Pt multilayer (symbols) shows a low-q and high-q peak. Only the low-q peak is field dependent. Power spectral density functions obtained from an x-ray microscope domain image and an atomic force microscope height profile are scaled vertically and plotted on the same q scale. (From Ref. 84.)

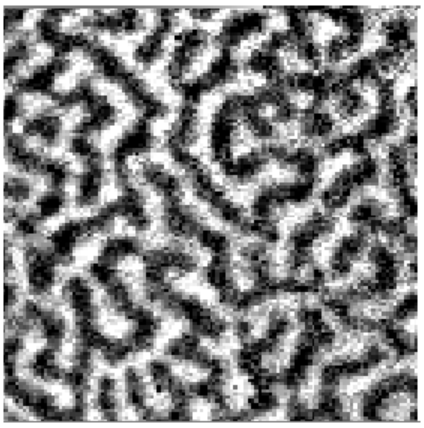

Figure 16. Imaging x-ray microscope domain image (4.5 μm field) from a Co/Pt multilayer similar to that whose scattering is in Figure 15.

shows values of f_c and f_{m1} across the Co $L_{2,3}$ resonances, where the measured f_2 parts yield the f_1 parts via the dispersion relation.

Since this scattering was measured using linear incident polarization, the theoretical model developed above predicts that the scattering contains only magnetic-magnetic and charge-charge contributions, with no charge-magnetic scattering. Thus, the low-q magnetic domain peak near remanence should be well modeled by the spectrum of $4f_{m1}^{*}f_{m1}$ for Co, as illustrated in the inset of Figure 18a that shows the pure magnetic scattering contrast between oppositely oriented domains. This scattering contrast reverses with helicity. The resonant absorption by the sample must be included in the model, which means multiplying the calculated scattering spectrum by the sample's transmission spectrum. Using measured values for f_{m1} yields good agreement with the measured peaks in the scattering spectrum at remanence, provided a small, non-resonant charge scattering background is added to fit the measured background away from the Co L lines. At saturation, this weak charge background is the only contribution to calculated scattering at the low-q peak.

To describe the charge scattering spectra from many possible models, it is reasonable to assume from the AFM results that topological interface roughness and/or density variations at polycrystalline grain boundaries are responsible for this scattering, and so that some linear combination of Co and Pt f_c should describe the scattering. Iterative modeling yields $a_c = f_{c,Co} + 3f_{c,Pt}$ for an amplitude that, when squared, produces good agreement with the measured spectrum at saturation in Figure 18b. (Note

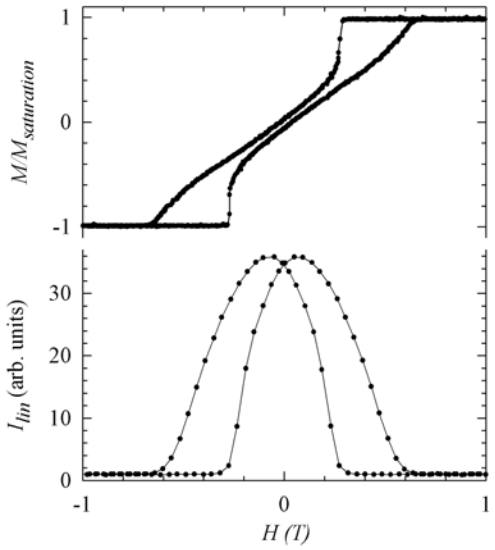

Figure 17. A SQUID easy axis hysteresis loop showing the average magnetization of a Co/Pt multilayer (top). Corresponding resonant scattering loop showing the strength of magnetization fluctuations (domains) at a fixed spatial frequency (bottom). (From Ref. 84.)

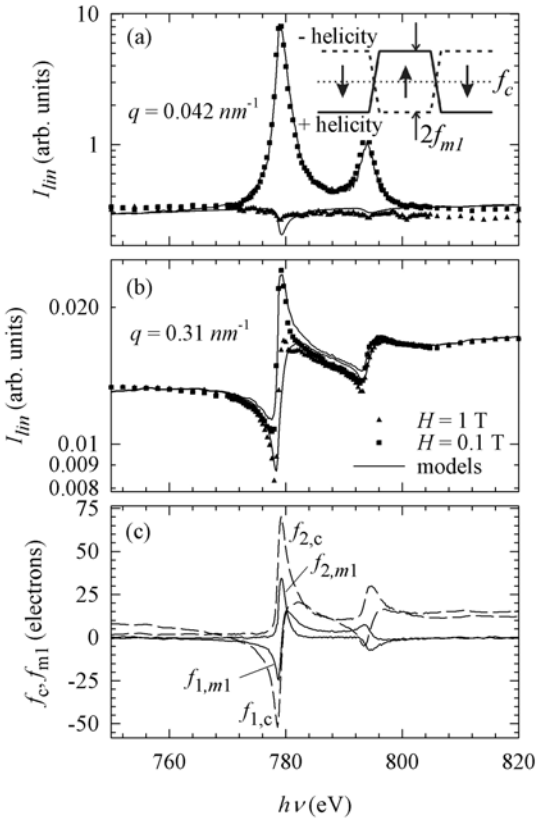

Figure 18. Energy spectra of scattering (symbols) at saturation and near remanence measured at the low-q domain peak and the high-q charge peak are in (a) and (b), respectively. The Co resonant charge and magnetic scattering factors in (c) are used to model the measured spectra above (lines). The inset in (a) shows the pure magnetic scattering contrast for oppositely oriented domains. (From Ref. 84.)

the characteristic bipolar shape of this pure charge scattering resonance, while the pure magnetic scattering resonance in Figure 18a has unipolar enhancements at each Co L line.) To model the scattering at the high-q peak near remanence, it was found that adding some pure magnetic intensity ($f_{m1}^{*} f_{m1}$) to this pure charge intensity produces good agreement. Such field-dependent pure magnetic intensity at the high-q peak is reasonably expected to be associated with the chemical density variation of Co. It was impossible to improve the agreement between model and data at the high-q peak with an added charge-magnetic interference term. Thus, these modeling results at both the low- and high-q peaks are consistent with the theoretical prediction that only pure magnetic and pure charge intensities contribute to I_{lin}.

Co/Pt multilayers and similar films with perpendicular anisotropy provide model systems to study **M** structure in films whose energetics are altered by introducing perpendicular exchange-bias [85], antiferromagnetic coupling [86], microstructural disorder [87], lithographic patterning [88], and domain order [89]. Resonant scattering

has been used to follow the effects of these interactions on domain structure and reversal behavior. Such modifications may be important in future generations of perpendicular magnetic recording media and other devices.

5.3. Magnetic and chemical correlation lengths in recording media

While the transmission geometry is optimized to study magnetic structure in films with perpendicular anisotropy because of its overwhelming sensitivity to the $\mathbf{m}_x$ component, reduced magnetic sensitivity exists even when **M** is confined to the plane of the film as in Figure 14b. With $\mathbf{e}_0 = \mathbf{e}_\sigma$, for example, scattering from the $\mathbf{m}_z$ component scales as $\sin\theta$ in $\mathbf{e}_\sigma \rightarrow \mathbf{e}_\pi$ scattering. With $\mathbf{e}_0 = \mathbf{e}_\pi$, similar sensitivity exists to the $\mathbf{m}_z$ component in $\mathbf{e}_\pi \rightarrow \mathbf{e}_\sigma$ scattering, and to the $\mathbf{m}_y$ component in $\mathbf{e}_\pi \rightarrow \mathbf{e}_\pi$ scattering.

Scattering studies of recording media films with in-plane anisotropy have demonstrated this sensitivity to in-plane magnetization and provided the first direct measurements of magnetic correlation lengths in such films [90, 91, 92]. Recording media films are often termed granular alloy films because they are designed to chemically phase separate into nanometer scale grains whose centers are magnetic and whose grain boundaries are nominally non-magnetic. The chemical heterogeneity associated with these films is readily observed in transmission electron microscopy (TEM) [93], and small-spot electron energy loss spectroscopy (EELS) reveals that Cr segregates to the grain boundaries and Co segregates to the grain-centers. This heterogeneous microstructure functions by reducing exchange interactions between the magnetic grain centers, thereby allowing sharper bit transitions to be written and, consequently, higher recording density. The grain sizes are small enough, however, that the length scale over which magnetism is correlated between grains had been difficult to measure directly.

In traditional recording media alloys having in-plane anisotropy the magnetic Co and non-magnetic Cr both have accessible *L* edges for resonant scattering in the soft x-ray spectral range. Thus, in addition to field-dependent measurements to resolve charge (chemical) from magnetic heterogeneity as demonstrated above, measurements at these different edges can be used for the same purpose [90]. This is demonstrated in Figure 19, that shows *q* scans for three distinct, in-plane granular alloy media films measured with x-ray energy tuned to the Co and Cr L_3 resonances at 778 and 574 eV, respectively. These data were obtained using bending magnet radiation having a range of incident polarization states, for which theory implies that charge-charge, charge-magnetic, and magnetic-magnetic terms all contribute to measured intensities. Even so, at least a partial, qualitative distinction between these terms is obtained from the combined resonant scattering results at these two edges. Specifically, since Cr is known to exhibit negligible f_{m1} (from XMCD measurements), only chemical (charge-charge) correlations are expected when tuned to the Cr edge. (The implicit assumption that the Co f_{m1} term is small near the Cr resonance is valid.) However, near the Co L_3 resonance Co exhibits large enhancements in both f_c and f_{m1}, so that both charge and magnetic amplitudes contribute to scattering at this edge.

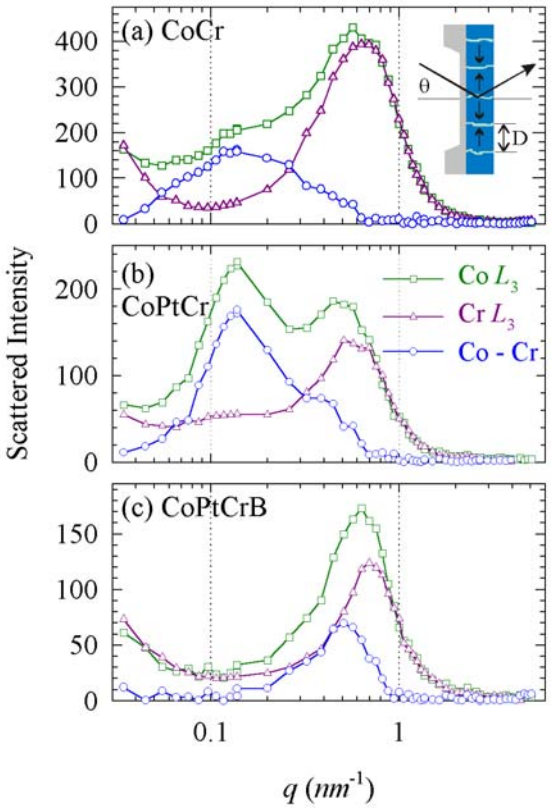

Figure 19. Scattered intensity vs. q for a series of Co-Cr based granular alloy recording media. Measurements are made at the Co and Cr L_3 edges, and are scaled to match at high q. The difference is also plotted. Data collected at the Cr edge result predominantly from pure charge correlations. Data collected at the Co edge contain both charge and magnetic contributions. The difference tends to isolate the magnetic contributions, revealing that magnetic correlation lengths are generally much longer than chemical correlation lengths in these materials, and that the addition of boron significantly reduces magnetic correlation lengths. (From Ref. 90.)

The three panels of Figure 19 correspond to a series of three recording media film compositions in the historical development of granular alloy media over the last decade or more. All films were grown on an identical underlayer structure. One or more peaks are observed in the resonant q scans for each sample. At the Cr edge a single peak predominates for each sample at $q \cong 0.7\ nm^{-1}$. This peak results from interference between adjacent scattering centers separated by $2\pi / q \cong 10\ nm$, consistent with intergrain separations observed in TEM images. Since it is known that Cr segregates to the grain boundaries, this peak clearly originates predominantly from chemical heterogeneity. At the Co edge the same interference peak is observed at $q \cong 0.7\ nm^{-1}$, and additional scattering is observed at significantly lower q. The high q scattering implies that this peak results from chemical segregation of Co and Cr. While at the Cr edge the scattering at the grain boundaries is enhanced, at the Co edge the scattering from the grain centers is enhanced. Thus these two complementary scattering structures produce essentially identical peaks, as they should since the Fourier transform of structure in a positive and negative black and white image is the same.

The additional scattering at lower q observed only at the Co edge must have a separate origin from the chemical segregation. In the CoCr and CoPtCr alloys a low q peak is observed at $q \cong 0.15\ nm^{-1}$, while in the CoPtCrB alloy the additional scattering essentially broadens the grain size peak to lower q. The data in Figure 18 are scaled so that Cr and Co edge data match on the high q side of the chemical grain peak. By subtracting the Cr from the Co edge scans theory implies that the remainder represents predominantly magnetic-magnetic and magnetic-charge correlations, both of which are expected to be strong for Co. These difference curves show a pronounced peak that is

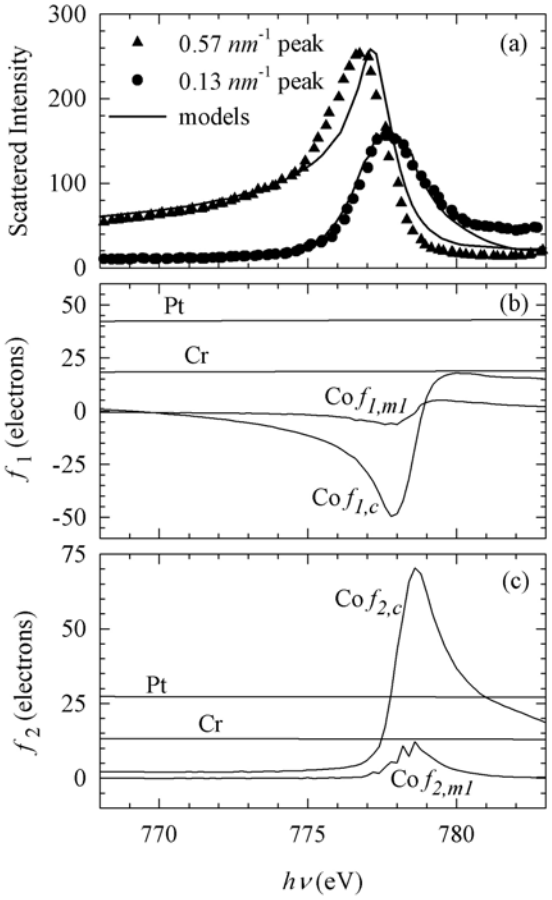

Figure 20. Co L_3 energy spectra at the low- and high-q peaks for the CoPtCr media sample are symbols in (a). The real and imaginary parts of scattering factors for Co, Cr, and Pt in (b) and (c), respectively, are used to produce the model spectra (lines) in (a). (From Ref. 91.)

well separated from the chemical grain size peak that is reasonably inferred to represent magnetic correlations, *i.e.*, interference between regions that have different average orientations of magnetization, based on scattering theory. The observation of distinct peaks in these difference curves implies that there is, on average, a characteristic magnetic correlation length describing the size of these magnetic regions.

To experimentally confirm the magnetic and chemical origin of the distinct peaks observed in Figure 19, one could measure changes with applied fields. However, these q scans were collected at remanence before the first application of an external field in order to study magnetic correlations in the as-grown state. While subsequent field dependent measurements do confirm the magnetic origin of the low-q peaks, initially this was determined by modeling energy scans across the Co L_3 edge collected at the two peaks of the CoPtCr sample, as shown in Figure 20. Like in the case of Co/Pt multilayers (above), the energy spectrum at the low-q peak of this granular alloy film can be well modeled by the shape of $f_{m1}^{*} f_{m1}$ plus a small, non-resonant background. No models involving added resonant chemical scattering fit the data as well as this pure resonant magnetic scattering model, thus establishing the low-q peak as pure magnetic in origin. The shape of this magnetic peak is determined solely by energy dependence of f_{m1}. It does not depend on the in-plane orientation of the magnetization of adjacent regions.

Modeling the high-q peak not only confirms its predominant origin from charge-charge correlations, but also provides a measure of the chemical segregation responsible

for this scattering. This modeling assumes a chemically segregated grain structure with Co-rich grain centers, and Co-deficient grain boundaries, consistent with prior knowledge from electron microscopy. Designating these two phases A and B, then the scattering amplitude of each phase will be a_A and a_B, where each represents a linear combination of the elemental atomic scattering factors weighted by their density in each phase. Figure 20b and 20c give the relevant scattering factors; the resonant Co values are measured and the non-resonant Cr and Pt values are taken from tabulated data [5]. The scattering amplitude contrast $a_{charge} = a_A - a_B$ then represents the scattering power of the chemically heterogeneous ensemble. The energy dependence of the scatter intensity $a^*_{charge} a_{charge}$ is clearly very sensitive to the chemical makeup of the two phases. Iterative evaluation of this spectra adjusting the composition of the two phases led to a model in which the Co-rich grain centers have Co:Pt:Cr ratio of 20:2:1, and the Co-deficient grain boundaries contain no Pt and have Co:Cr ratio of 1:1. The resulting spectral model is the dashed line in Figure 20a that reasonably accounts for the shape of the high-*q* peak. While it is not claimed that this pure charge scattering model is unique or yields the best possible fit to these data [91], these compositions are in reasonable agreement with expectations of composition based on focused EELS studies.

Thus there is good reason to believe that the low- and high-*q* features in Figure 19 do represent predominantly magnetic-magnetic and charge-charge correlations, respectively. The high-*q* chemical grain peaks are essentially constant in position with alloy composition, and represent the average intergrain distance or chemical correlation length scale. The magnetic peak, especially as evidenced in the difference curves, indicates that the magnetic correlation length remains substantially longer than the chemical grain size for both the CoCr and CoPtCr alloys. This in turn suggests that the magnetization of several adjacent grains tends to be correlated, presumably by undesirable intergrain exchange interactions. It is then deviations in magnetization orientation between regions containing several correlated grains that gives rise to the magnetic scattering observed at the low-*q* peak. With the addition of boron, however, the magnetic correlation length decreases significantly so that the difference peak closely approaches the chemical grain size peak.

Thus resonant magnetic scattering reveals directly that boron addition is highly effective in reducing intergrain magnetic exchange interactions. This correlates with improved signal to noise and recording density of the more complex alloy system. In addition to resolving magnetic correlation lengths, chemical correlation lengths are observed simultaneously, and careful modeling can provide meaningful measures of composition differences between chemically segregated regions at lengths scales of order 10 *nm* and below.

5.4. Coherent magnetic scattering

An x-ray beam's coherence is characterized by its longitudinal or temporal coherence length (along the propagation direction) and its transverse coherence length (normal to the propagation direction). A monochromatic plane wave constitutes a fully coherent beam. The longitudinal coherence length $\lambda^2 / \Delta\lambda$ is typically set by the resolving power of a grating monochromator in the soft x-ray region to have a value ~ 1000 – 10000 λ, and tends to be large compared to absorption lengths in general. The

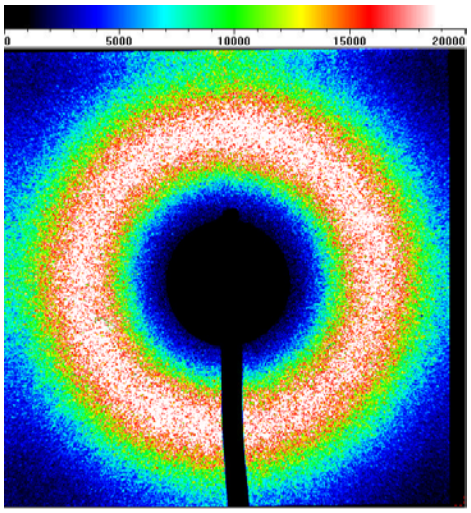

Figure 21. CCD image of the diffuse scattering ring produced by disordered stripe domains in a Co/Pt multilayer. An upstream spatial filter was used to enhance the speckle that can be seen within the smooth scattering envelop. A beam stop support is seen at the bottom. (From Ref. 87.)

transverse coherence scales as λ^2 over the source brightness, which for undulators at 3rd generation synchrotron sources can be appreciable [2]. While coherent x-ray scattering was first studied in the hard x-ray range [94], the λ^2 scaling makes the soft x-ray range especially attractive for coherent scattering studies [95].

The scattering discussed in the previous section is sometimes termed incoherent. However, it actually uses the coherence of the beam in two ways. The temporal coherence aids in tuning to specific resonant energies. The interference of scattering from inhomogeneities to produce peaks in reciprocal space can only occur for real space structure within the beam's coherence volume. Thus incoherent scattering is a misnomer, and partially coherent scattering is a more apt description. Even so, this partially coherent scattering ignores one important feature resulting from the coherence of the beam – the speckled intensity distribution of the scattering.

Coherent scattering refers to the use of incident radiation having a high degree of transverse coherence, *i.e.*, plane wave fronts. The phases of waves scattered across the plane wave front interfere in the far field (at the detector) to produce a speckled intensity pattern within the envelope function of the partially coherent intensity peaks discussed above. The intensity variation or contrast of the speckle is in principle 100% for fully coherent illumination. The degree of coherence is often augmented by positioning a pinhole (spatial filter) between the source and sample. The speckle encodes the complete local details of the 2-dimensional spatial distribution of scattering centers, and thus contains far more information that just the position and width of the interference peaks as discussed above. To measure the speckled intensity distribution, a detector with spatial resolution finer than the speckle size is needed. Often a charge-coupled device (CCD) detector is used for this purpose.

Magnetic speckle has been observed in several x-ray studies [80, 96, 88, 87] although is in its infancy at the time of this writing. Figure 21 shows an example of a magnetic speckle pattern obtained from Co/Pt multilayers identical to those discussed above. The diffuse ring of intensity in this CCD image is the same magnetic peak in Figure 15, resulting from labyrinth stripe domains like those in Figure 16. Examination of the scattering reveals speckles that extend over one or two CCD pixels, so the oversampling of the intensity peak is just sufficient. Just as the mechanisms of coherent

magnetic scattering are direct extensions of visible coherent techniques, so are the general types of information obtainable from these techniques. The information contained in magnetic speckle can be used in several different ways.

In principle the speckle distribution can be inverted to obtain a real-space image of the scattering object. In practice, phasing the speckle pattern can be problematic in this form of lenseless imaging, although oversampling the speckle pattern and the use of known boundary conditions to the scattering object can overcome the phase problem [97]. Attempts to perform this inversion with magnetic speckle have been carried out using real [98] and simulated data [98, 99]. Initial results are promising, although expected concerns about the uniqueness of resulting images are not currently resolved. Rapid advances in speckle inversion via holographic or heterodyning approaches, that interfere the speckle pattern with a known reference wave, can be anticipated [100, 101]. The lenseless imaging approach is being investigated as an imaging mode for fourth generation synchrotron x-ray sources operating in single-shot mode.

The second approach is the x-ray analog of dynamic light scattering, time (or photon) correlation spectroscopy, or intensity fluctuation spectroscopy initially developed using lasers. Here, temporal intensity fluctuations in the solid angle of a single speckle provide information about sample dynamics at that spatial frequency. X-ray time correlation spectroscopy was first applied in the hard x-ray [102, 103], where time resolution down to 50 nanoseconds has been obtained [104]. In the soft x-ray it has been used in dynamic, non-resonant, charge scattering down to microsecond time resolution in liquid crystals [95]. Studies of magnetization dynamics with microsecond or possibly better time resolution should be feasible.

A third approach to utilizing coherent magnetic scattering is similar to time correlation spectroscopy in that it relies on changes in magnetic speckle, but now with respect to field-induced, quasi-static changes in domain structure rather than rapid spontaneous fluctuations [87]. Very different from dynamic fluctuation spectroscopies, this speckle metrology approach uses a large portion of the coherent scattering pattern containing many speckles. Correlation coefficients are defined such that the auto-correlation of a static speckle pattern yields 1, while the cross-correlation of two uncorrelated speckle patterns yields 0. So defined, the cross-correlation coefficient of two speckle patterns obtained at different points around a hysteresis loop provides a direct statistical measure of the ensemble-averaged domain correlations between these two measurements. Speckle metrology is thus an ideal tool to measure microscopic magnetic domain memory in films. Compared to speckle inversion, this approach sidesteps the phase uniqueness question to obtain statistical microscopic correlations. Compared to soft x-ray microscopy (below) and other magnetic microscopies, this approach forgoes specific local real space information about individual domains in favor of a statistical value over all of real space sampled.

Domains in Co/Pt multilayer films were the first objects studied by magnetic speckle metrology. Specifically, two multilayers of similar nominal structure, [Co(0.4 *nm*)/(Pt 0.7 *nm*)]$_{50}$, but sputter deposited at 3 and 12 *millitorr* argon pressure were investigated [87]. The visible MOKE hysteresis loops for these two samples in Figure 22 show that the two films have significantly different reversal behavior. While domains mediate reversal in each film, their remanence and coercivity depend sensitively on the relative amount of microstructural disorder that in turn depends on the sputter pressure.

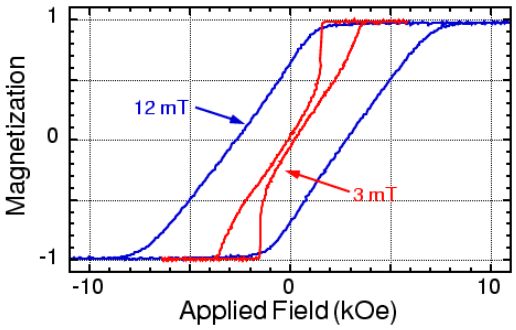

Figure 22. Visible MOKE hysteresis loops for Co/Pt multilayers sputter deposited at two different argon pressures reveal very different reversal mechanisms. (From Ref. 87.)

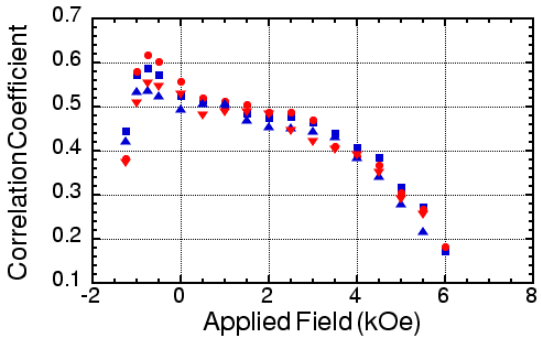

Figure 23. Cross correlation coefficients obtained at the same applied field point after one or more complete hysteresis loop cycles reveal the trend in microscopic return point domain memory for the 12 mTorr sample. (From Ref. 87.)

Films deposited at lower pressure tend to be smoother than those deposited at higher pressure; the extreme roughness limit corresponds to columnar growth of polycrystalline grains with voided grain boundaries, while the smooth limit corresponds to a polycrystalline microstructure with dense grain boundaries and a relatively smooth surface topography [105]. Speckle metrology reveals that the extent of microscopic magnetic memory is dramatically different depending on the growth-induced disorder in these films. Return-point memory of the domain configurations is quantified by the cross-correlation coefficient between speckle patterns measured at the same field point on a hysteresis loop, but following one or many minor or major loop excursions away from the initial point.

Consider first the return-point memory when the end points are at the coercive point, where M = 0 and many domains are present. It was found that the smooth sample exhibited finite memory for minor loops that stopped short of saturation [87]. However, once saturation was reached in minor or major loops, all return-point memory of domain structure was lost. This is consistent with essentially random nucleation and growth of domains from saturation in the smooth sample. The rougher, 12 *millitorr* sample, on the other hand, exhibited non-zero return-point memory for both minor loops to saturation and major loops. Figure 23 shows the RPM for major loops for this sample, where the x-axis corresponds to the starting and ending field at which the cross-correlations were evaluated. The sharp onset of memory at negative fields corresponds to the initial nucleation of domains in a loop starting from negative saturation. Following the nucleation peak, the cross-correlation remains high as domain growth and wall motion proceeds, before falling to zero as saturation is approached. Thus, while domain nucleation exhibits strong memory, as domains proliferate their distribution becomes more random. This characteristic shape of the memory vs. endpoint H is retained for cross-correlations between tens of major loops, indicating that the increased structural disorder contains numerous pinning sites that influence both nucleation and growth of domains in a very robust way.

Its relatively direct and quantitative statistical measure of microscopic magnetic memory of a large structural ensemble suggests that the speckle metrology technique will become a useful tool in studying a variety of magnetic systems where details of the reversal mechanism are of interest. Magnetic storage media are one example, where the interplay between structural and magnetic disorder are expected to have a strong bearing on signal-to-noise and related device performance issues. In addition to this new form of speckle metrology, it is expected that lenseless imaging and time correlation spectroscopy using coherent magnetic scattering will grow as the limits of their capabilities are more fully established.

6. Direct magnetization imaging

Several different approaches for direct (real space) magnetic imaging have been developed utilizing resonant XMCD and XMLD to gain sensitivity to ferromagnetic and antiferromagnetic structure. These are broadly categorized as electron imaging microscopes and zone-plate microscopes that utilize x-rays entirely to form images.

6.1. Photo-electron emission microscopes

One approach images low energy (secondary) electrons emitted from a magnetic surface, much as in the SPLEEM technique discussed in Chapter 9. Rather than using spin-polarization detection, however, magnetic contrast is gained through the XMCD or XMLD effects on the secondary emission, requiring incident tunable soft x-rays of suitable polarization [106, 107, 108, 109]. Such photo-emission electron microscopes (PEEMs) have routine spatial resolution of ~ 50 *nm* set by chromatic aberrations of imaging secondary electrons. Elaborate schemes to improve this resolution down to ~ 1-2 *nm* are under investigation. The extreme sensitivity to surface magnetic properties of secondary emission enables the study of smooth surfaces and layers buried under only 2-3 *nm* of material. Short, pulsed fields applied between synchrotron x-ray pulses are feasible, and have been used to study magnetization dynamics in confined thin films [110, 111]. Static applied fields orthogonal to the nominal electron trajectory are incompatible with low energy electron imaging. Other limitations include the inability to study layers and interfaces several nanometers or more below the surface and samples that are insulating or have surface topography that yields unwanted contrast.

These properties make PEEMs especially powerful to study exchange bias systems, where XMCD and XMLD contrast allows imaging of ferromagnetic and antiferromagnetic domains, respectively, in the same sample [112,113]. In addition to spatial resolution, quantitative spectroscopy can provide detailed information about the anisotropy axes in different layers [114] and interfacial spins [115].

6.2. Imaging and scanning zone-plate microscopes

Two distinct types of soft x-ray zone-plate microscopes, full field imaging and scanning, have been utilized to image magnetic structure. Their fundamental components are illustrated in Figure 24. High-resolution Fresnel zone plate lenses are at the heart

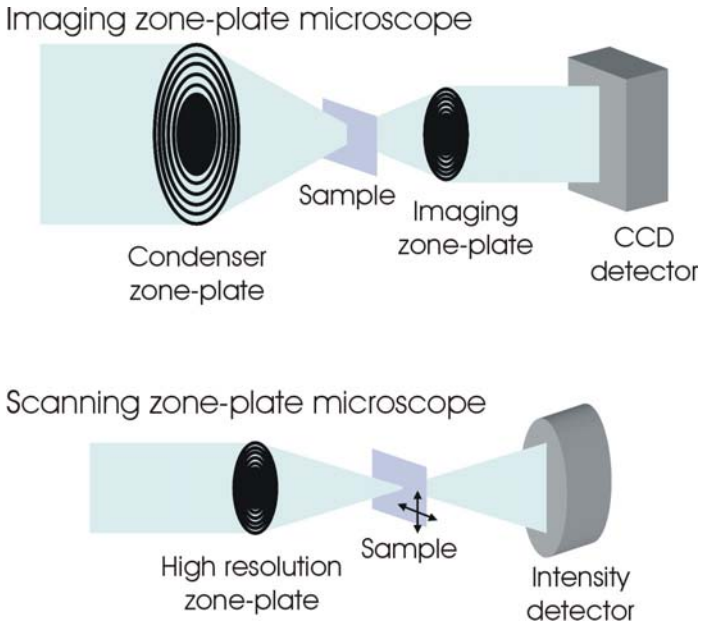

Figure 24. Two different microscope configurations using zone-plate lenses to image magnetization.

these microscopes. These ultrafine diffracting structures require state-of-the-art electron beam lithography to precisely position concentric circular rings over large areas forming the physical aperture of the lens [2, 116]. The diffraction-limited spatial resolution offered by a simple zone-plate lens approximately equals $1.22\delta r_N$ where δr_N is the width of the outermost zone. For current lithography technology the diffraction limited spatial resolution is 18-30 nm.

Full field imaging microscopes require a condenser optic to illuminate the sample, followed by a high resolution zone plate to project an image onto a 2-dimensional detector [117, 118]. Coarse resolution zone plate lenses are often used as the condenser, although focusing mirror condensers may also serve this purpose.

Scanning transmission zone-plate microscopes utilize a single high-resolution zone-plate lens to focus a high-brightness incident beam to a diffraction-limited spot. The sample is raster-scanned through the focal spot, and the transmitted intensity is monitored. An order-sorting aperture slightly smaller than the opaque central region of the lens is positioned to aperture most of the radiation not diffracted in first order (focused) by the zone plate. Compared to a limited field of view of an imaging microscope, the field of a scanning microscope is limited only by the scanning stages.

Both types of zone-plate microscopes obtain magnetic contrast via the XMCD effect in transmission absorption. Transmission geometry requires freestanding samples or samples on semitransparent substrates. For samples with magnetization in the substrate plane, the sample must be tilted away from normal incidence to obtain magnetic contrast ($\propto p_{m1}$), while samples with perpendicular anisotropy are easily studied at normal incidence.

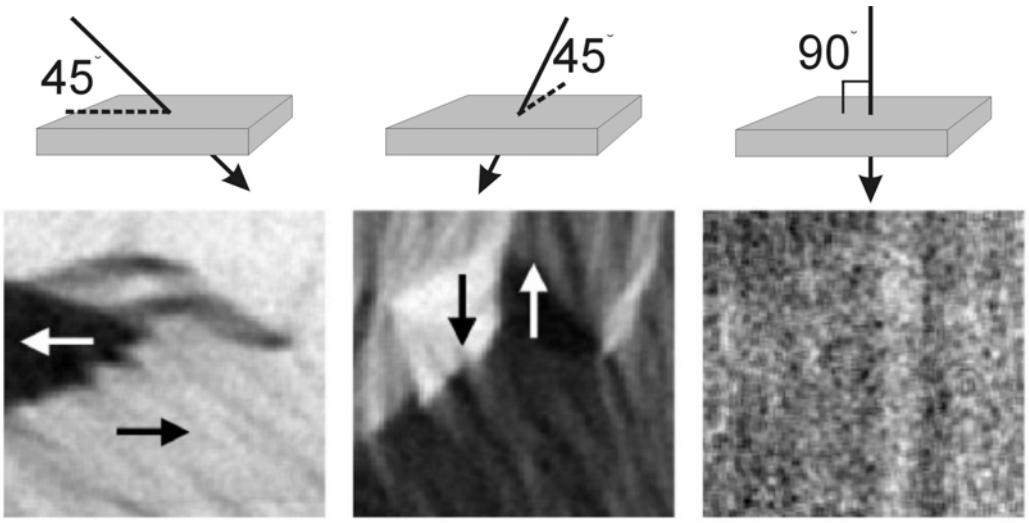

Figure 25. Scanning transmission x-ray microscope images of the same 60 x 60 μ*m* region of a demagnetized, 33 *nm* thick Fe film taken at three viewing angles as indicated. Each image is actually the division of two images obtained with opposite helicity elliptical polarization tuned to the Fe L_3 line to enhance magnetic contrast. These projections of *M* variation along the beam direction reveal a blade-shaped domain growing from the left into a larger 180° domain. Arrows indicate *M* orientation along projected directions. (From Ref. 126.)

6.3. Zone-plate imaging of domain structure

The first SXR images of magnetic structure studied stripe domains in Gd/Fe multilayers having perpendicular anisotropy [119, 120], much like those in Figure 16. Such studies have expanded to include patterned films with perpendicular anisotropy [118, 121, 122], field-dependent domain behavior [123, 89], and extended [124] and patterned films having in-plane anisotropy.

The first magnetic images from a scanning transmission x-ray microscope (STXM) [125] were of domain and domain-boundary structures in demagnetized films having in-plane anisotropy [38, 126]. Since tilting is required to obtain XMCD contrast for in-plane *M*, it is simple to extend tilting to multiple viewing angles in order to reconstruct the vector nature of magnetization resolved laterally across a film. This is demonstrated in Figure 25, where three images show black and white XMCD contrast images obtained at viewing angles as indicated from a demagnetized, 33 *nm* thick Fe film [126]. Seen in these images is a needle- or blade-shaped domain growing into a larger region of nominally reversed magnetization. Since the contrast in these images results from the projection of **M** along the viewing direction, the data is readily transformed to obtain the direction of **M**, as seen in Figure 26. The main image shows in-plane **M** components that are color-coded to represent directions as indicated. The inset shows perpendicular **M** components, with separate color scale indicating the angle out of plane (90 indicates in-plane *M*). A rich variety of structure is observed at and near the grain boundary, including hybrid Néel and Bloch domain walls, pronounced perpendicular magnetization components at the core of vortex structures, and vortex pairs extending

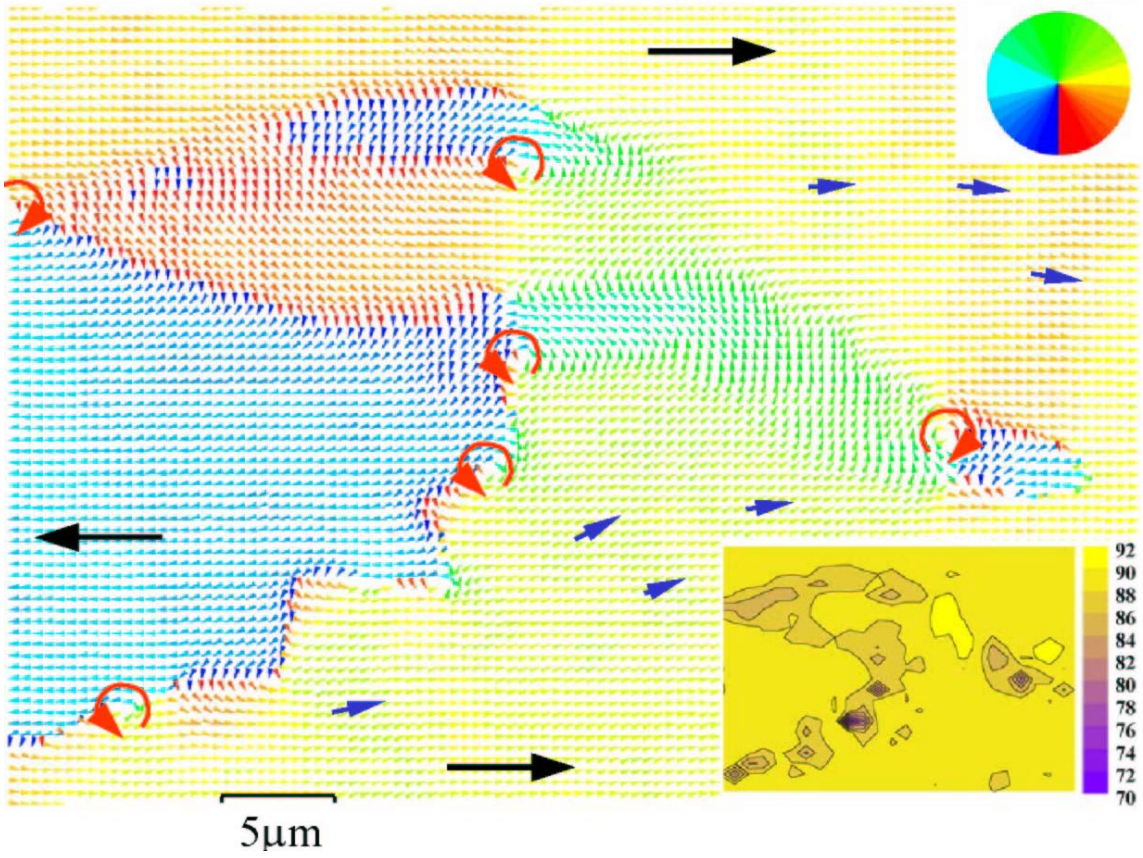

Figure 26. Composite 50 x 35 μ*m* image of vector magnetization at the tip of blade domain growing into a 180° domain. The main image shows in-plane magnetization, with arrows and color wheel indicating in plane directions. The inset shows out-of-plane magnetization components, with 90° corresponding to in-plane. (From Ref. 126.)

well away from the main domain wall. While these structures were known to exist before this study, the improved spatial resolution coupled with quantitative vector imaging capabilities are expected to yield new information on a range of magnetic features as they become more routinely used.

To date, zone-plate microscopes have been developed primarily for polymer and wet chemical and biological studies, not for magnetic studies. Implementing limited sample tilting and applied magnetic field capabilities has been feasible in these existing microscopes. Future zone-plate microscopes specifically designed for magnetic studies would enable stronger applied fields, sample temperature control, more flexible transmission geometries, and reflection geometry studies. Dynamic studies using pump-probe techniques are compatible with both microscopes [127]. The high flux density in the focused STXM spot should enable interesting time correlation experiments analogous to dynamic light scattering using coherent scattering, only now in a small, well-defined sample volume.

6.4. Complementarity of microscopy and scattering

The results presented above raise questions concerning the relative utility of scattering vis-à-vis microscopy to study magnetic heterogeneity since, after all, microscopy was used to image (Figure 16) the same domains whose low q scattering was measured in both partially coherent (Figure 15) and more fully coherent (Figure 21) fashion. Of course, microscopy and scattering have complementary sensitivity to magnetic heterogeneity. Images provide direct, detailed information about local magnetic structure, especially isolated or individual features, that is unavailable from scattering. Thus real space images are tremendously valuable because of their specific information content and because of the ease with which it is grasped. The correlation functions from scattering, on the other hand, typically average over a larger ensemble than do images to provide (arguably) a statistically more robust measure of certain types of structure. Scattering is inherently a dark field technique, and its very origin makes it extremely sensitive to magnetic heterogeneity. Zone plate x-ray microscopy is a bright-field technique, and so has somewhat different, albeit large, sensitivity to magnetic heterogeneity.

In addition to these well-known attributes, specific differences are emerging as relevant in their comparative capabilities. Spatial resolution in zone-plate microscopy scales as the inverse of the zone-plate numerical aperture that is difficult to increase beyond ~ 0.1. Scattering can be measured out to backscattering with an effective numerical aperture ($\propto q$) of 1, and so can resolve features ten times smaller than microscopy. This larger spatial frequency range over which signals are inherently Fourier filtered, coupled with a larger dynamic range, gives scattering significantly greater sensitivity to mixed heterogeneity than microscopy. For example, simultaneous sensitivity to magnetic and chemical structure below the zone-plate resolution limit has been obtained in scattering measurements of granular recording media [91, 128, 129]. The more open geometry of scattering experiments may make them more amenable to utilization in a variety of sample environments.

Of course, the combination of scattering and microscopy generally provide more information that either technique in isolation.

7. Summary

In summary, relevant core resonances for 3*d* transition and 4*f* rare earth elements provide elemental, electronic state, spin, and orbital moment sensitivity to spectroscopies in the soft x-ray spectral region. These are driving the extension of the entire variety of spectroscopic, scattering, and microscopy techniques familiar from other spectral regions into the soft x-ray region, that in turn brings nanometer scale sensitivity to magnetically and chemically heterogeneous systems. While these developments are still in progress, numerous studies have already demonstrated that the attributes of these soft x-ray techniques can impact our understanding of a variety of important systems. Their general applicability to interfaces, thin films and near surface properties of bulk samples suggests that their application will expand. Dynamic and time-resolved techniques, also familiar from other spectral ranges, are beginning to be combined with these unique capabilities

offered by the soft x-ray spectral range. It is reasonable to expect that these techniques will all continue to evolve to provide increasing understanding of magnetic systems and phenomena of fundamental and technological interest.

8. Acknowledgements

The author would like to acknowledge collaborators E. E. Fullerton, O. Hellwig, S.-K. Kim, S. Jiang, S. D. Bader, L. Sorensen, S. D. Kevan, G. P. Denbeaux, T. Warwick and K. M. Chesnel for their contributions to work described in this chapter, and for many stimulating discussions. The work at LBNL was supported by the Director, Office of Energy Research, Office of Basic Energy Sciences, U. S. Department of Energy under Contract No. DE-AC03-76SF00098.

9. References

[1] J. B. Kortright, D. D. Awschalom, J. Stöhr, S. D. Bader, Y. U. Idzerda, S. S. P. Parkin, I. K. Schuller, and H.-C. Seigmann, J. Magn. Magn. Mater. **207**, 7 (1999).
[2] D. T. Attwood, Soft x-rays and extreme ultraviolet radiation: principles and applications, Cambridge University Press, Cambridge (2000).
[3] J. J. Sakurai, Advanced quantum mechanics, Addison-Wesley, Reading, Mass. (1967).
[4] R. W. James, The optical principles of the diffraction of x-rays, Ox Bow Press, Woodbridge, Connitecut, 1982.
[5] B. L. Henke, E. M. Gullikson, and J. C. Davis, At. Data and Nucl. Data Tables, **54** (1993), 181, and X-Ray Data Booklet, http://xdp.lbl.gov.
[6] J. P. Hannon, G. T. Trammel, M. Blume, and D. Gibbs, Phys. Rev. Lett. **61**, 1245 (1988), and errata, *ibid*, **62**, 2644 (1989).
[7] S. W. Lovsey and S. P. Collins, X-Ray Scattering and Absorption in Magnetic Materials, Oxford University Press, Oxford, 1996.
[8] D. Gibbs, D. R. Harshman, E. D. Isaacs, D. B. McWhan, D. Mills, and C. Vettier, Phys. Rev. Lett. **61**, 1241 (1989).
[9] K. Chesnel, M. Belakhovsky, A. Marty, G. Beutier, G. van der Laan, and S. P. Collins, Physica B **345**, 148 (2004).
[10] J. B. Kortright and S.-K. Kim, Phys. Rev. B **62**, 12216 (2000).
[11] J. E. Prieto, F. Heigl, O. Krupin, G. Kaindl, and K. Starke, Phys. Rev. B **68**, 134453 (2003).
[12] J. Stöhr, NEXAFS Spectroscopy, Springer-Verlag, Berlin, (1992).
[13] F. M. F. de Groot, J. C. Fuggle, B. T. Thole, and G. A. Sawatzky, Phys. Rev. B **42**, 5459 (1990).
[14] B. T. Thole, G. van der Laan, and G. A. Sawatzky, Phys. Rev. Lett. **55**, 2086 (1985).
[15] G. Schütz, W. Wagner, W. Wilhelm, P. Kienle, R. Zeller, R. Frahm, and G. Materlik, Phys. Rev. Lett. **58**, 737 (1987).
[16] B. T. Thole, P. Carra, F. Sette, and G. van der Laan, Phys. Rev. Lett. **68**, 1943 (1992).
[17] P. Carra, B. T. Thole, M. Altarelli, and X. Wang, Phys. Rev. Lett. **70**, 694 (1993).

[18] C. T. Chen, Y. U. Idzerda, H.-J. Lin, N. V. Smith, G. Meigs, E. Chaban, G. H. Ho, E. Pellegrin, and F. Sette, Phys. Rev. Lett. **75**, 152 (1995).
[19] R. Nakajima, J. Stöhr, Y. U. Idzerda, Phys. Rev. B. **59**, 6421 (1999).
[20] D. Weller, J. Stöhr, R. Nakajima, A. Carl, M. G. Samant, C. Chappert, R. Mégy, P. Beauvillain, P. Veillet, and G. A. Held, Phys. Rev. Lett. **75**, 3752 (1995).
[21] J. Stöhr and H. König, Phys. Rev. Lett. **75**, 3748 (1995).
[22] L. Néel, J. Phys. Radium **15**, 376 (1954).
[23] Y. Wu, J. Stöhr, B. D. Hermsmeier, M. G. Samant, and D. Weller, Phys. Rev. Lett. **69**, 2307 (1992).
[24] M. Samant, J. Stöhr, S. S. P. Parkin, G. A. Held, B. D. Hermsmeier, F. Herman, M. van Schilfgaarde, L.-C. Duda, D. C. Mancini, N. Wassdahl, and R. Nakajima, Phys. Rev. Lett. **72**, 1112 (1994).
[25] M. Tischer, O. Hjortstam, D. Arvanitis, J. Hunter Dunn, F. May, K. Baberschke, J. Trygg, J. M. Wills, B. Johansson, and O. Eriksson, Phys. Rev. Lett. **75**, 1602 (1995).
[26] N. Nakajima, T. Koide, T. Shidara, H. Miyauchi, H. Fukutani, A. Fujimori, K. Iio, T. Katayama, M. Nývlt, and Y. Suzuki, Phys. Rev. Lett. **81**, 5229 (1998)
[27] S.-K. Kim and J. B. Kortright, Phys. Rev. Lett. **86**, 1347 (2001).
[28] G. van der Laan, Phys. Rev. Lett. **82**, 640 (1999).
[29] R. Wienke, G. Schütz, H. Ebert, J. Appl. Phys. **69**, 6147 (1991).
[30] S. Pizzini, A. Fontaine, C. Giorgetti, E. Dartyge, J.-F. Bobo, M. Piecuch, B. Baudelet, Phys. Rev. Lett. **74**, 1470 (1995).
[31] F. Wilhelm, P. Poulopoulos, G. Ceballos, H. Wende, K. Baberschke, P. Srivastava, D. Benea, H. Ebert, M. Angelakeris, N. K. Flevaris, D. Niarchos, A. Rogalev, and N. B. Brookes, Phys. Rev. Lett. **85**, 413 (2000).
[32] S.-K. Kim, J.-R. Jeong, J. B. Kortright, and S.-C. Shin, Phys. Rev. B **64**, 052406 (2001).
[33] D. J. Keavney, D. Wu, J. W. Freeland, E. Johnston-Halperin, D. D. Awschalom, and J. Shi, Phys. Rev. Lett. **91**, 187203 (2003).
[34] J.-Y. Kim, J.-H. Park, B.-G. Park, H.-J. Noh, S.-J. Oh, J. S. Yang, D.-H. Kim, S. D. Bu, T.-W. Noh, H.-J. Lin, H.-H. Hsieh, and C. T. Chen, Phys. Rev. Lett. **90**, 017401 (2003).
[35] F. M. F. de Groot, M. A. Arrio, Ph. Sainctavit, Ch. Cartier, and C. T. Chen, Solid State Com. **92**, 991 (1994).
[36] M. van Veenendaal, J. B. Goedkoop, and B. T. Thole, Phys. Rev. Lett. **77**, 1508 (1996).
[37] M. O. Krause, J. Phys. Chem. Ref. Data **8**, 307 (1979).
[38] J. B. Kortright, M. Rice, S.-K. Kim, C. C. Walton, and T. Warwick, J. Magn. Magn. Mater. **191**, 79 (1999).
[39] J. B. Kortright, J. Magn. Magn. Mater. **156**, 271 (1996).
[40] J. B. Kortright, M. Rice, and K. D. Frank, Rev. Sci. Instrum. **66**, 1567 (1995).
[41] M. Yanagihara, T. Maehara, H. Nomura, M. Yamamoto, T. Namioka, and H. Kimura, Rev. Sci. Instrum. **63**, 1516 (1992).
[42] F. Schäfers, H. C. Mertins, A. Gaupp, W. Gudat, M. Mertin, I. Packe, F. Schmolla, S. Di Fonzo, G. Soullie, W. Jark, R. Walker, X. Le,Cann, R. Nyholm, M. Eriksson, Applied Optics **38**, 4074 (1999).

[43] J. B. Kortright and J. H. Underwood, Nucl. Instrum. Meth. A **291**, 272 (1990).
[44] J. B. Kortright, H. Kimura, V. Nikitin, K. Mayama, M. Yanagihara, and M. Yamamoto, Appl. Phys. Lett. **60**, 2963 (1992).
[45] J. B. Kortright, S.-K. Kim, T. Warwick, and N. V. Smith, Appl. Phys. Lett. **71**, 1446 (1997).
[46] J. B. Kortright, M. Rice, and R. Carr, Phys. Rev. B **51**, 10240 (1995).
[47] H. C. Mertins, F. Schäfers, X. Le Cann, A. Gaupp, and W. Gudat, Phys. Rev. B. **61**, R874 (2000).
[48] R. Wu and A. J. Freeman, J. Appl. Phys. **79**, 6500 (1996).
[49] A. Scherz, H. Wende, K. Babershke, J. Minár, D. Benea, and H. Ebert, Phys. Rev B, **66**, 184401 (2002).
[50] H. Ebert and S. Man'kovsky, Phys. Rev. Lett. **90**, 077404 (2003).
[51] H.-C. Mertins, P. M. Oppeneer, J. Kuneš, A. Gaupp, D. Abramsohn, and F. Schäfers, Phys. Rev. Lett. **87**, 047401 (2001).
[52] J. Kuneš, P. M. Oppeneer, H.-C. Mertins, F. Schäfers, A. Gaupp, W. Gudat, and P. Novak, Phys. Rev. B **64**, 174417 (2001).
[53] V. N. Antonov, B. N. Harmon and A. N. Yaresko, Phys. Rev. B **67**, 024417 (2003).
[54] M. J. Frieser, IEEE Trans. Mag. **4**, 152 (1968).
[55] H. Ebert, Rep. Prog. Phys. **59**, 1665 (1996).
[56] J. Zak, E. R. Moog, C. Liu, and S. D. Bader, Phys. Rev. B **43**, 6423 (1991).
[57] Z. Q. Qiu and S. D. Bader, Rev. Sci. Instrum. **71**, 1243 (2000).
[58] C. Kao, J. B. Hastings, E. D. Johnson, D. P. Siddons, G. C. Smith, and G. A. Prinz, Phys. Rev. Lett. **65**, 373 (1990).
[59] J. M. Tonnerre, L. Sève, D. Raoux, G. Soullié, B. Rodmacq, and P. Wolfers, Phys. Rev. Lett. **75**, 740 (1995).
[60] J. B. Kortright, M. Rice, S.-K. Kim, C. C. Walton, and T. Warwick, J. Magn. Magn. Mater. **191**, 79 (1999).
[61] J. B. Kortright, S.-K. Kim, E. E. Fullerton, J. S. Jiang, and S. D. Bader, Nucl. Instrum. Meth. A **467**, 1396 (2001).
[62] P. M. Oppeneer, H.-C. Mertins, O. Zaharko, J. Phys. Cond. Mat. **15**, 7803 (2003).
[63] H.-C. Mertins, S. Valencia, D. Abramsohn, A. Gaupp, W. Gudat, and P. M. Oppeneer, Phys. Rev. B **69**, 064407 (2004).
[64] K. Starke, F. Heigl, A. Vollmer, M. Weiss, G. Reichardt, and G. Kaindl, Phys. Rev. Lett. **86**, 3415 (2001).
[65] M. Sacchi, A. Mirone, C. F. Hague, P. Castrucci, R. Gunnella, and M. De Crescenzi, Phys. Rev. B **64**, 012403 (2001).
[66] Y. U. Idzerda, V. Chakarian, and J. W. Freeland, Phys. Rev. Lett. **82**, 1562 (1999).
[67] P. M. Oppeneer, H.-C. Mertins, D. Abramsohn, A. Gaupp, J. Kuneš, and C. M. Schneider, Phys. Rev. B **67**, 052401 (2003).
[68] S. Gider, B.-U. Runge, A. C. Marley, and S. S. P. Parkin, Science **281**, 797 (1998).
[69] E. F. Kneller and R. Hawig, IEEE Trans. Magn. **27**, 3588 (1991).
[70] R. Skomski and J. M. D. Coey, Phys. Rev. B **48**, 15812 (1993).
[71] E. E. Fullerton, J. S. Jiang, and S. D. Bader, J. Magn. Magn. Mater. **200**, 392 (1999).
[72] J. B. Kortright, J. S. Jiang, S. D. Bader, O. Hellwig, D. T. Marguiles, and E. E. Fullerton, Nucl. Instrum. Meth. B **199**, 301 (2003).

[73] O. Hellwig, J. B. Kortright, K. Takano, and E. E. Fullerton, Phys. Rev. B **62**, 11694 (2000).
[74] K. Amemiya, S. Kitagawa, D. Matsumura, T. Yokoyama, and T. Ohta, J. Phys.: Condens. Matter **15**, S561 (2003).
[75] K.-S. Lee, S.-K. Kim, and J. B. Kortright, Appl. Phys. Lett. **83**, 3764 (2003).
[76] J. F. MacKay, C. Teichert, D. E. Savage, and M. G. Lagally, Phys. Rev. Lett. **77**, 3925 (1996).
[77] J. W. Freeland, V. Chakarian, K. Bussmann, and Y. U. Idzerda, J. Appl. Phys. **83**, 6290 (1998).
[78] R. M. Osgood III, S. K. Sinha, J. W. Freeland, Y. U. Idzerda, and S. D. Bader, J. Magn. Magn. Mater. **198-199**, 698 (1999).
[79] S. K. Sinha, E. B. Sirota, S. Garoff, and H. B. Stanley, Phys. Rev. B **38**, 2297 (1988).
[80] A. Rahmim, S. Tixier, T. Tiedje, S. Eisebitt, M. Lörgen, R. Scherer, W. Eberhardt, J. Lüning, and A. Scholl, Phys. Rev. B **65**, 235421 (2002).
[81] J. B. Kortright, O. Hellwig, S. Sun, and E. E. Fullerton, submitted for publication.
[82] H. A. Dürr, E. Dudzik, S. S. Dhesi, J. B. Goedkoop, G. van der Laan, M. Belakhovsky, C. Mocuta, A. Marty, and Y. Samson, Science **284**, 2166 (1999).
[83] E. Dudzik, S. S. Dhesi, S. P. Collins, H. A. Dürr, G. van der Laan, K. Chesnel, M. Belakhovsky, A. Marty, Y. Samson, and J. B. Goodkoep, J. Appl. Phys. **87**, 5469 (2000).
[84] J. B. Kortright, S.-K. Kim, G. P. Denbeaux, G. Zeltzer, K. Takano, and E. E. Fullerton, Phys. Rev. B **64**, 092401 (2001).
[85] O. Hellwig, S. Maat, J. B. Kortright, and E. E. Fullerton, Phys. Rev. B **65**, 144418 (2002).
[86] O. Hellwig, T. L. Kirk, J. B. Kortright, A. Berger, and E. E. Fullerton, Nature Materials, **2**, 112 (2003).
[87] M. S. Pierce, R. B. Moore, L. B. Sorensen, S. D. Kevan, E. E. Fullerton, O. Hellwig, and J. B. Kortright, Phys. Rev. Lett. **90**, 175502 (2003).
[88] K. Chesnel, M. Belakhovsky, F. Livet, S. P. Collins, G. van der Laan, S. S. Dhesi, J. P. Attané, and A. Marty, Phys. Rev. B **66**, 172404 (2002).
[89] O. Hellwig, G. P. Denbeaux, J. B. Kortright, and E. E. Fullerton, Physica B **336** (2003) 136.
[90] O. Hellwig, D. T. Margulies, B. Lengsfield, E. E. Fullerton, and J. B. Kortright, Appl. Phys. Lett. **80**, 1234 (2002).
[91] J. B. Kortright, O. Hellwig, D. T. Marguiles, and E. E. Fullerton, J. Magn. and Magn. Mater. **240**, 325 (2002).
[92] E. E. Fullerton, O. Hellwig, K. Takano, and J. B. Kortright, Nucl. Instrum. Meth. B **200**, 202 (2003).
[93] M. Doerner, X. Bain, M. Madison, K. Tang, Q. Peng, A. Polcyn, T. Arnoldussen, M. F. Toney, M. Mirzamaani, K. Takano, E. E. Fullerton, M. Schabes, K. Rubin, M. Pinarbase, S. Yuan, M. Parker, and D. Weller, IEEE Trans. Magn. **34**, 1564 (2001).
[94] M. Sutton, S. G. J. Mochrie, T. Greytak, S. E. Nagler, L. E. Berman, G. A. Held, and G. B. Stephenson, Nature **352**, 608 (1991).
[95] A. C. Price, L. B. Sorensen, S. D. Kevan, J. Toner, A. Poniewierski, and R. Holyst, Phys. Rev. Lett. **82**, 755 (1999).

[96] F. Yakhou, A. Létoublon, F. Livet, M. de Boissieu, and F. Bley, J. Magn. Magn. Mater. **233**, 119 (2001).
[97] J. Miao, P. Charalambous, J. Kirz, and D. Sayre, Nature **400**, 342 (1999).
[98] A. Rahmim, M.Sc. Thesis, University of British Columbia (1999).
[99] T. O. Menteş, C. Sánchez-Hanke, and C. C. Kao, J. Synchrotron Radiation **9**, 90 (2002).
[100] S. Eisebitt, M. Lörgen, W. Eberhardt, J. Lüning, S. Andrews, and J. Stöhr, Appl. Phys. Lett. 84, 3373 (2004).
[101] S. Eisebitt (private communication).
[102] G. Brauer, G. B. Stephenson, M. Sutton, R. Brüning, E. Dufrense, S. G. J. Mochrie, G. Grübel, J. Als-Nielsen, and D. L. Abernathy, Phys. Rev. Lett. **74**, 2010 (1995).
[103] S. Dierker, R. Pindak, R. M. Flemming, I. K. Robinson, and L. Berman, Phys. Rev. Lett, **75**, 449 (1995).
[104] I. Sikharulidze, I. P. Dolbnya, A. Fera, A. Madsen, B. I. Ostrovskii, and W. H. de Jeu, Phys. Rev. Lett. **88**, 115503 (2002).
[105] E. E. Fullerton, J. Pearson, C. H. Sowers, S. D. Bader, X. Z. Wu, and S. K. Sinha, Phys. Rev. B **48**, 17432 (1993).
[106] J. Stöhr, Y. Wu, B. D. Hermsmeier, M. G. Samant, G. R. Harp, D. Dunham, and B. P. Tonner, Science **259**, 658 (1993).
[107] C. M. Schneider and G. Schonhense, Reports on Progress in Physics **65**, R1785 (2002).
[108] S. Anders, H. Padmore, R. M. Duarte. T. Renner, T. Stammler, A. Scholl, M. R. Scheinfein, J. Stöhr, L. Sève, and B. Sinkovic, Rev. Sci. Instrum. **70**, 3973 (1999).
[109] W. Kuch, L. I. Chelaru, F. Offi, M. Kotsugi, and J. Kirschner, J. Vac. Sci. Technol. B **20**, 2543 (2002).
[110] J. Vogel, W. Kuch, M. Bonfim, J. Camarero, Y. Pennec, F. Offi, K. Fukumoto, J. Kirschner, A. Fontaine, and S. Pizzini, Appl. Phys. Lett. **82**, 2299 (2003).
[111] S.-B. Choe, Y. Acermann, A. Scholl, A. Bauer, A. Doran, J. Stöhr, and H. A. Padmore, Science **304**, 420 (2004).
[112] A. Scholl, J. Stöhr, J. Lüning, J. W. Seo, J. Fompeyrine, H. Siegwart, J. P. Locquet, F. Nolting, S. Anders, E. E. Fullerton, M. R. Scheinfein, and H. A. Padmore, Sience **287**, 1014 (2000).
[113] W. Kuch, L. I. Chelaru, F. Offi, J. Wang, M. Kotsugi, and J. Kirschner, Phys. Rev. Lett. **92**, 017201 (2004).
[114] H. Ohldag, A. Scholl, F. Nolting, S. Anders, U. Hillebrecht, and J. Stöhr, Phys. Rev. Lett. **86**, 2878 (2001).
[115] H. Ohldag, T. J. Regan, J. Stöhr, A. Scholl, F. Nolting, J. Lüning, C. Stamm, S. Anders, and R. L. White, Phys. Rev. Lett. **87**, 7201 (2001).
[116] R. Tatchyn, P. L. Csonka, and I. Lindau, J. Opt. Soc. Am. B **1**, 806 (1984).
[117] G. Schmahl, D. Rudolph, P. Guttmann, G. Schneider, J. Thieme, and B. Niemann, Rev. Sci. Instr. **66,** 1282 (1995).
[118] G. Denbeaux, P. Fischer, G. Kusinski, M. Le Gros, A. Pearson, and D. Attwood, IEEE Trans. Magn. **37**, 2764 (2001).
[119] P. Fischer, G. Schütz, G. Schmahl, P. Guttmann, and D. Raasch, J. de Physique IV **7-C2**, 467 (1997).

[120] P. Fischer, T. Eimüller, G. Schütz, P. Guttmann, G. Schmahl, K. Pruegl, G. Bayreuther, J. Phys. D: Appl. Phys. **31**, 649 (1998).
[121] T. Eimüller, P. Fischer, G. Schütz, M. Scholz, G. Bayreuther, P. Guttmann, G. Schmahl, M. Köhler, J. Appl Phys. **89**, 7162 (2001).
[122] G. J. Kusinski, K. M. Krishnan, G. Denbeaux, G. Thomas, G. Denbeaux, B. D. Terris, and D. Weller, Appl. Phys. Lett. **79**, 2211 (2001).
[123] P. Fischer, G. Denbeaux, T. Eimuller, D. Goll, and G. Schütz, IEEE Trans. Magn., **38**, 2427 (2002).
[124] P. Fischer, T. Eimüller, G. Schütz, M. Köhler, G. Bayreuther, G. Denbeaux, and D. Attwood, J. Appl. Phys. **89**, 7159 (2001).
[125] T. Warwick, H. Ade, S.Cerasari, J. Denlinger, K. Franck, A. Garcia, S. Hayakawa, A. Hitchcock, J, Kikuma, S. Klingler, J. Kortright, G. Morisson. M. Moronne, E. Rightor, E. Rotenberg, S. Seal, H.J. Shin. W. F. Steele, and B. P. Tonner, Journal of Synchrotron Radiation **5**, 1090 (1998).
[126] S.-K. Kim, J. B. Kortright, and S.-C. Shin, Appl. Phys. Lett. **78**, 2724 (2001).
[127] P. Fischer (private communication).
[128] O. Hellwig, D. T. Marguiles, B. Lengsfield, E. E. Fullerton, and J. B. Kortright, Appl. Phys. Lett. **80**, 1234 (2002).
[129] E. E. Fullerton, O. Hellwig, Y. Ikeda, B. Lengsfield, K. Takano, and J. B. Kortright, IEEE Trans. Magn. **38**, 1693 (2002).